*Article*

# Vegetation Subtype Classification of Evergreen Broad-Leaved Forests in Mountainous Areas Using a Hierarchy-Based Classifier

**Shiqi Zhang [1,2], Peihao Peng [3,\*], Maoyang Bai [1,2], Xiao Wang [4], Lifu Zhang [5], Jiao Hu [1], Meilian Wang [6], Xueman Wang [1], Juan Wang [3], Donghui Zhang [5], Xuejian Sun [5] and Xiaoai Dai [1]**

1   College of Earth Sciences, Chengdu University of Technology, Chengdu 610059, China
2   Department of Geosciences and Geography, University of Helsinki, 00014 Helsinki, Finland
3   College of Tourism and Urban-Rural Planning, Chengdu University of Technology, Chengdu 610059, China
4   School of Architecture and Civil Engineering, Chengdu University, Chengdu 430072, China
5   Aerospace Information Research Institute, Chinese Academy of Sciences, Beijing 100094, China
6   Department of Land Surveying and Geo-Informatics, Hong Kong Polytechnic University, Hongkong 999077, China
\*   Correspondence: pengpeihao@cdut.edu.cn; Tel.: +86-133-4089-4347

**Abstract:** Evergreen broad-leaved forests with rich biodiversity play a key role in stabilizing global vegetation productivity and maintaining land carbon sinks. However, quantitative and accurate classification results for humid, evergreen, broad-leaved forests (HEBF) and semi-humid evergreen broad-leaved forests (SEBF) with different vegetation productivity and significant differences in species composition are lacking. Remote sensing technology brings the possibility of vegetation subtype classification. Taking the mountainous evergreen broad-leaved forests distributed in Sichuan Province as an example, this study proposed a hierarchy-based classifier combined with environmental variables to quantitatively classify the two vegetation subtypes with different ecological characteristics but similar image features. Additionally, we applied Sun–Canopy–Sensor and C parameter(SCS + C) topographic correction to preprocess the images, effectively correcting the radiometric distortion and enhancing the accuracy of vegetation classification. Finally, achieving an overall accuracy (OA) of 87.91% and a Kappa coefficient of 0.76, which is higher than that of directly using the classifier to classify the two vegetation subtypes. The study revealed the widespread distribution of evergreen broad-leaved forests in Sichuan, with a clear boundary between the distribution areas of HEBF and SEBF. The HEBF in the east is located in the basin and the low marginal mountains; the SEBF is located in the southwest dry valley. The methods employed in this study offer an effective approach to vegetation classification in mountainous areas. The findings can provide guidance for ecological engineering construction, ecological protection, and agricultural and livestock development.

**Keywords:** vegetation classification; semi-humid evergreen broad-leaved; humid evergreen broad-leaved forest; remote sensing; hierarchy-based classifier

## 1. Introduction

Evergreen broad-leaved forests are characteristic zonal vegetation in subtropical regions, hosting abundant biodiversity and playing a critical role in stabilizing global vegetation productivity and maintaining land carbon sinks under more intense climate extremes in the future [1,2]. In China, the evergreen broad-leaved forests have the widest distribution, occupy the most extensive area, and display remarkable complexity and diversity [3,4], yet they have been subject to drier soil and more frequent droughts over the recent decades [5,6]. The scientific and rational mapping and classification of evergreen broad-leaved forests serve as a fundamental approach to comprehending the spatial distribution, structure

characteristics, and species composition and evaluating their ecological functions and ecosystem services.

In China, evergreen broad-leaved forests are classified into two vegetation subtypes, namely, the semi-humid evergreen broad-leaved forests (SEBF) and the humid evergreen broad-leaved forests (HEBF). The classification principle is established by differentiating the ecological characteristics of the HEBF and SEBF vegetation, such as variations in group species, which were identified through extensive field investigations [7–9]. This classification is qualitative and preliminary, originating from labor-intensive, time-consuming, and expensive manual field surveys conducted in the 1980s. Hence, this classification is qualitative and preliminary, derived from labor-intensive, time-consuming, and expensive manual field surveys conducted in the 1980s. Presently, numerous research stations established by the International Biological Program (IBP) have provided indications of differences in vegetation productivity between HEBF and SEBF [10–14]. However, there is still no quantitative classification of the HEBF and SEBF. Additionally, an accurate map of vegetation subtypes serves as the foundation for estimating the ecological benefits of evergreen broad-leaved forests and developing an optimal model for regional sustainable development.

Vegetation classification involves grouping different vegetation types based on their similarity. Geographically, each unit of vegetation classification is characterized by scattered and discontinuous distribution, often exhibiting a generalized and abstract [15,16]. Remote sensing technology offers robust support for vegetation distribution range assessment, mapping, forestry resources survey, and monitoring. It provides comprehensive coverage, a large amount of information, and a short update cycle [17–19]. The underlying principle involves utilizing classifiers to differentiate various vegetation types based on spectral, texture, and temporal features extracted from remote sensing images, thereby generating thematic vegetation maps. However, global remote sensing dataset products, such as GLC_FCS30 [20], MCD12Q1 [21], GCL2000v1.1, and UMD Land Cover [22], are only classified into vegetation type (e.g., evergreen broad-leaved forest or evergreen coniferous forest), and there is no remote sensing dataset classified into vegetation subtypes (the HEBF and SEBF). Optical remote sensing images with higher spatial resolution, such as Landsat 8 and sentinel-2A data, show promise in detecting differences in vegetation properties [23,24]. Different combinations and calculations of spectral bands can capture distinct vegetation conditions, leading to the development of various vegetation indices, including the normalized difference vegetation index (NDVI), the improved soil–atmosphere corrected vegetation index (EVI), Tasseled Cap Transformation, etc. [25–27]. Furthermore, Synthetic Aperture Radar (SAR) is extensively employed due to its all-weather, all-day, and high-resolution remote sensing capabilities. Moreover, it is also proved that Sentinel-1 SAR contains vegetation structure features, which are complementary to optical [28,29]. In addition, variations in environmental variables, such as climate, geomorphology, and moisture, lead to subdividing the same vegetation type into different subtypes. These environmental variables play a crucial role in shaping the spatial distribution of vegetation [7]. Therefore, they serve as significant reference data for vegetation classification, enhancing the accuracy of the classification process [30–32].

Meanwhile, machine learning algorithms have gained popularity in vegetation classification for extracting vegetation features. These algorithms, such as maximum likelihood [33], K-nearest neighbor (KNN) [34], Support Vector Machine (SVM) [35,36], Random Forest (RF) [37,38], Gradient Tree Boosting (GTB) [39], leverage the full potential of remote sensing images. Moreover, traditional vegetation remote sensing classification studies the impact of different classifiers on accuracy, typically involving the direct extraction of spectral information from multiple vegetation types within a complex area. However, native evergreen broad-leaved forests are often widely distributed in mountainous areas with diverse vegetation types, posing challenges in extracting individual vegetation types and classifying their subtypes from complex backgrounds [40,41]. In recent years, hierarchy-based classifiers have emerged as a solution to the classification and extraction challenges posed by complex backgrounds. These classifiers can be organized into different

layers based on distinct vegetation features, offering greater expressiveness and flexibility compared to single classifiers [42–46]. Additionally, current research on mountain vegetation classification predominantly concentrates on small areas or specific mountains [46,47]. The challenge arises from the variation in spectral information caused by the topographic undulations of the mountains, significantly impacting the accuracy of vegetation extraction information. Topographic correction is commonly used to mitigate radiometric distortions caused by topography in remote sensing images [48,49]. Existing methods involve transforming the radiance or reflectance of all image elements to a reference plane (typically horizontal) and then minimizing the variations in image values caused by topographic relief. This approach aims to enhance the capture of spectral characteristics. The primary objective of topographic correction is to derive the radiance values that the sensor would have measured on a perfectly flat surface [50,51]. Numerous studies have highlighted the crucial importance of topographic correction in improving land classification [52], particularly in the extraction and classification of vegetation information in mountainous areas. The topographic correction has become an indispensable preprocessing step for vegetation classification in mountain remote sensing [50,53,54]. Topographic correction models have been proposed, mainly classified into empirical, semi-empirical, and physical models [46,49,51]. Among them, semi-empirical models are simple and have physical meaning, and they require the introduction of the Digital Elevation Model (DEM) to assist in the correction [55]. These methods assume a Lambertian surface and may neglect the Bidirectional Reflectance Distribution Function (BRDF) effect or employ empirical parameters for topographic corrections [56]. The Sun–Canopy–Sensor and C parameter(SCS + C) correction is a semi-empirical terrain correction model Sun–Canopy–Sensor correction model that considers the upward growth characteristics of trees in forest cover scenes. However, the topographic correction of remote sensing images is mainly performed for single-view images [57]. With the advancement of remote sensing research and commercialization, cloud computing is one of the most powerful big data technologies. The Google Earth Engine (GEE https://developers.google.com/earth-engine/, accessed on 27 April 2023) cloud computing platform brings the possibility of topographic correction for large areas [58,59]. Thus, it has a great potential to classify into HEBF and SEBF in mountainous areas.

The evergreen broad-leaved forest in Sichuan province is the most important vegetation in horizontal zonality and the baseband vegetation in vertical zonality [60–62]. The study aims to provide a quantitative and accurate classification of the HEBF and SEBF subtypes in the mountainous evergreen broad-leaved forests of Sichuan Province, China. A hierarchy-based classifier combined with environmental variables is proposed for the classification, while SCS + C topographic correction is applied to improve classification accuracy. The findings of this research enhance the understanding of the spatial distribution, structure, and composition of HEBF and SEBF and provide valuable insights for ecological engineering, ecological protection, and agricultural and livestock development in mountainous areas.

## 2. Materials and Method

### 2.1. Study Area

Sichuan Province, with an area of 486,000 km$^2$, is located in southwestern China (longitude 97°30'~110°10'E, latitude 26°02'~34°20'N), in the transition zone between the Tibetan Plateau and the middle-lower Yangtze River Plain (Figure 1). The eastern part of Sichuan Province is occupied by the well-known Sichuan Basin, while the western part consists of plateaus and high mountain valleys. The Sichuan Basin is surrounded by mountains, including the Micang Mountains and Daba Mountains in the North, the Wushan and Qiyao Mountains in the east and southeast, the Dalou Mountains in the south, and the Longmen Mountains, Emei Mountains, and the large and small Liangshan Mountains in the west and southwest. The elevation of these mountains generally ranges

from 1500 to 2000 m, with Wushan and Daloushan being exceptions and mostly below 2000 m in elevation.
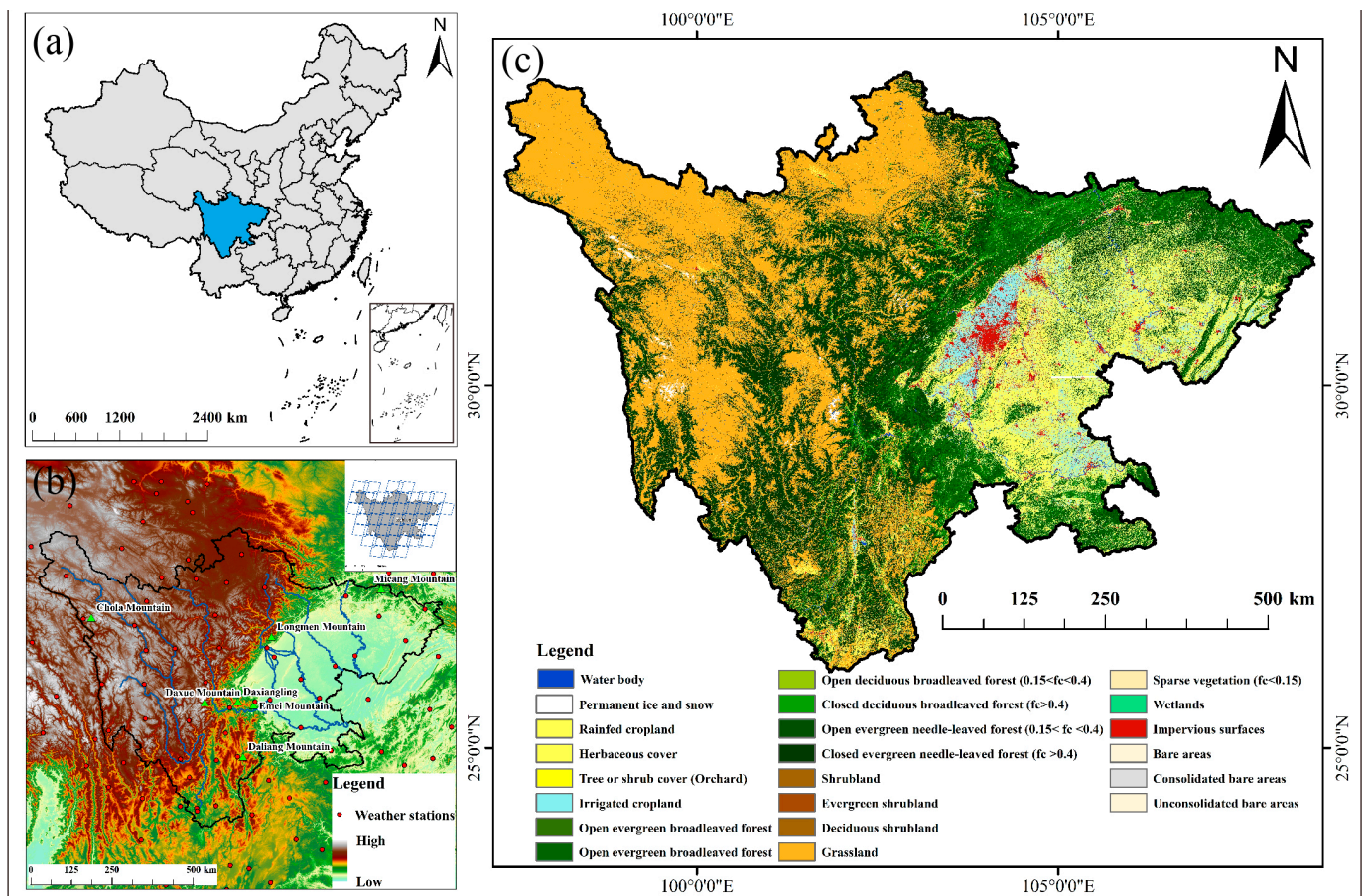


**Figure 1.** The geographical overview of the study area. (**a**) Location of the study area in China. (**b**) Digital elevation model map of the study area. (**c**) Global Land Cover with a Fine Classification System at 30 m in 2020 of the study area [20].

Eastern and southwestern parts of Sichuan Province are home to extensive evergreen broad-leaved forests characterized by diverse community species composition, including endemic tree species in China. The alpine valleys of western Sichuan are dominated by flourishing subalpine coniferous forests, primarily consisting of endemic tree species in western China. In northwestern Sichuan, the plateaus are covered with scrub and meadows specially adapted to alpine habitats (Figure 1). As mentioned in the 2000 publication "*Vegetation in Sichuan*": the group species of HEBF contains *Phoebe zhennan*, *Polyspora speciose*, *Castanopsis carlesii*, *Castanopsis eyrei*, *Castanopsis fargesii*, *Castanopsis platyacantha*, *Schima sinensis*, *Schima argentea*, *Machilus microcarpa*, *Cyclobalanopsis glauca*, and *Lithocarpus cleistocarpus*. While the group species of SEBF contains *Cyclobalanopsis gracilis*, *Castanopsis delavayi*, *Lithocarpus cleistocarpus*, and other *Fagaceae* family plants (the Latin texts of the vegetation mentioned above are in the Flora of China classification system) [63].

### 2.2. Data Sources

#### 2.2.1. Datasets

In this study, remote sensing images from three datasets were utilized (Table 1): Landsat 8 Level 2 Collection 2 Tier 1, Sentinel-1 Ground Range Detected (GRD) scenes, and NASADEM. Landsat 8 Level 2 Collection 2 Tier 1 is a reflectance product created by the Land Surface Reflectance Code (LaSRC) and processed by a single-pass algorithm. It was used as a vegetation classification image feature and to invert land surface temperature

as an environmental variable. Sentinel-1 GRD scenes is an ortho-corrected product that was processed using Sentinel-1 Toolbox to generate calibrated data and was used as a vegetation classification image feature. NASADEM is a reprocessing of STRM data with improved accuracy by incorporating auxiliary data from ASTER GDEM, ICESat GLAS, and PRISM datasets. It provides terrain information through topographic correction and environmental variables such as elevation, slope, and aspect. All these datasets were preprocessed and made available on the Google Earth Engine (GEE https://developers. google.com/, accessed on 27 April 2023) cloud platform.

**Table 1.** Detail information on datasets.

| Datasets | Spatial Resolution | Temporal Resolution |
|---|---|---|
| Landsat 8 | 30 m | 16 days |
| Sentinel-1 | 10 m | 12 days |
| NASADEM | 30 m | |
| Precipitation data | | Monthly |
| Sunshine duration data | | Monthly |

Additionally, monthly meteorological data on precipitation and sunshine duration obtained from 105 meteorological stations in Sichuan Province and surrounding regions were acquired from the China Meteorological Science Data Sharing Service (http://cdc. cma.gov.cn/, accessed on 27 April 2023). These data were incorporated as environmental variables in the classification process to enhance the accuracy of classification results.

2.2.2. Field Data

A vegetation survey was conducted in Sichuan Province from 2018 to 2020 to analyze survey density and sample distribution, which is highly significance for vegetation distribution mapping. The survey was conducted in three phases. In the first phase, the forest was stratified using Google Earth imagery on the OvitalMap mobile application (https://www.ovital.com/tg-guge/, accessed on 27 April 2023) and recording field-based geolocations with OvitalMap. The second phase involved recording 10 m × 10 m sample plots with central coordinates, community composition, and dominant species. The dominant species present in each condition were identified and recorded as vegetation types. The field data were organized in the third phase according to the recorded vegetation type, and the sample plots were classified into four vegetation classification levels based on the Flora of China classification system. The determination method involved identifying whether the sample plot belongs to the evergreen forests, evergreen broad-leaved forests, HEBF, or SEBF. As shown in Figure 2, 6866 sample plots were collected, representing almost all vegetation types in Sichuan Province.

*2.3. Data Preprocessing*

2.3.1. Images Preprocessing

- Image compositing

There were significant differences between the HEBF and SEBF in the dry and wet seasons. Using the Operational Land Imager (OLI) on-board Landsat 8, forty-three coverages (comprising five Bands from Band 2 to Band 7) were selected in the study area. All available remote sensing images from 1 May 2020 to 30 September 2020 were filtered for the least cloudiness and highest quality and then composited to form the dry season images of the entire study area. Similarly, all available remote sensing images from 1 November 2019 to 31 March 2020 were filtered for the least cloudiness and highest quality and then composited to form the wet season images of the entire study area. The information on filtered coverages information for the synthetic dry and wet seasons images is provided in Appendix A (Tables A1 and A2). Subsequently, cloud removal was performed using the

"QA_PIXEL" band in Landsat SR provided by Google Earth Engine (GEE), and the images were interpolated for the null values after cloud removal.
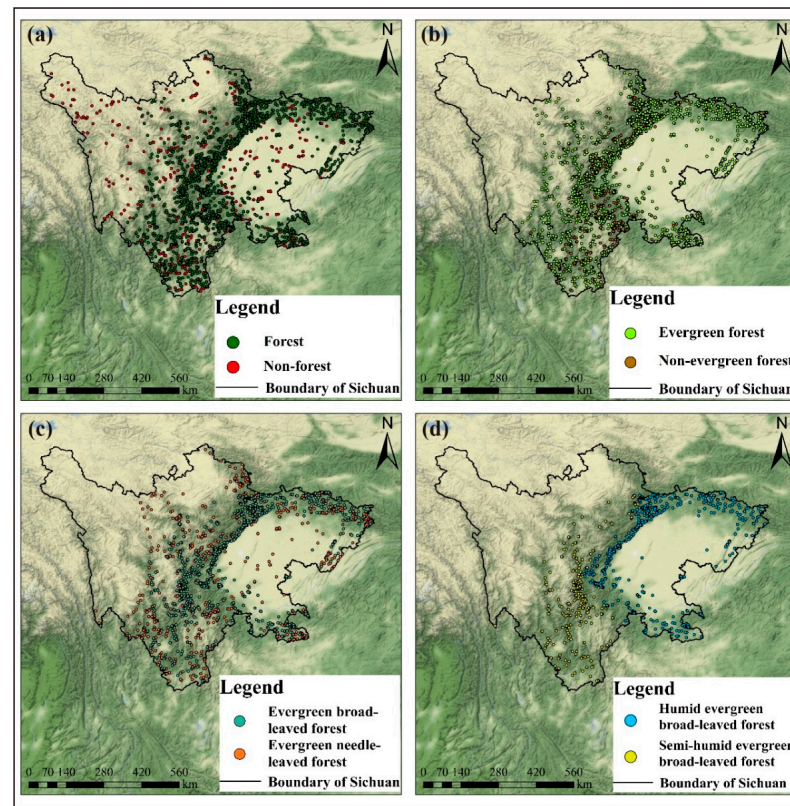


**Figure 2.** The spatial distribution map of the samples. (**a**). Samples distribution of forest and non-forest. (**b**). Samples distribution of evergreen forests and non-evergreen forest. (**c**). Samples distribution of evergreen broad-leaved forest and evergreen needleleaved forest. (**d**). Samples distribution of HEBF and SEBFThis method is standard for the Sichuan Wildlife Survey and Protection Project (No.80303-KZZ031).

- Topographic correction

The topographic effects of medium and high-resolution remote sensing images can significantly impede the application of remote sensing images for vegetation classification in mountainous areas. Topographic correction can partially mitigate the impact of topography, resulting in parameters that are more consistent with the reflection and radiation characteristics of the natural ground surface. Soenen et al. [57] proposed the modified Sun–Canopy–Sensor (SCS + C) topographic correction method, which combines the Sun–Canopy–Sensor (SCS)) [64] with a semi-empirical moderator (C) to account for diffuse radiation. The results of their study suggest that SCS + C should be considered for the topographic correction of remote sensing imagery in forested terrain, as expressed by Equation (1).

$$\rho_n = \rho \frac{\cos \alpha \cos \theta + C}{\cos i + C} \tag{1}$$

where $\rho_n$ is the reflectance after topographic correction, $\rho$ is the reflectance before topographic correction, $\alpha$ is the slope angle of the plane where the image element is located, $\theta$ is the solar zenith angle, $i$ is the solar incidence angle, and C is an empirical parameter.

The cosine of the solar incidence angle ($i$) in Equation (2):

$$\cos i = \cos a \cos q + \sin a \sin q \cos(j - b) \tag{2}$$

where $\varphi$ is the solar azimuth angle; $\beta$ is the aspect angle of the terrain.

The parameter C can be found from the linear relationship between the reflectance and the cosine of the incident angle before topographic correction and the linear relationship in Equation (3):

$$\rho = a + b \cos i \tag{3}$$

where *a* is the intercept of the linear Equation and *b* is the slope of the linear Equation. The parameter C can be calculated by fitting the intercept *a* and slope *b* of Equation (3). The parameter C can be calculated in Equation (3)

$$C = \frac{a}{b} \tag{4}$$

Additionally, the NASADEM was used to provide $\alpha$ and $\beta$, $\theta$ and $i$ are the header file of Landsat 8 provided. The before and after topographic correction of the study area for Landsat 8 is shown in Figure 3.
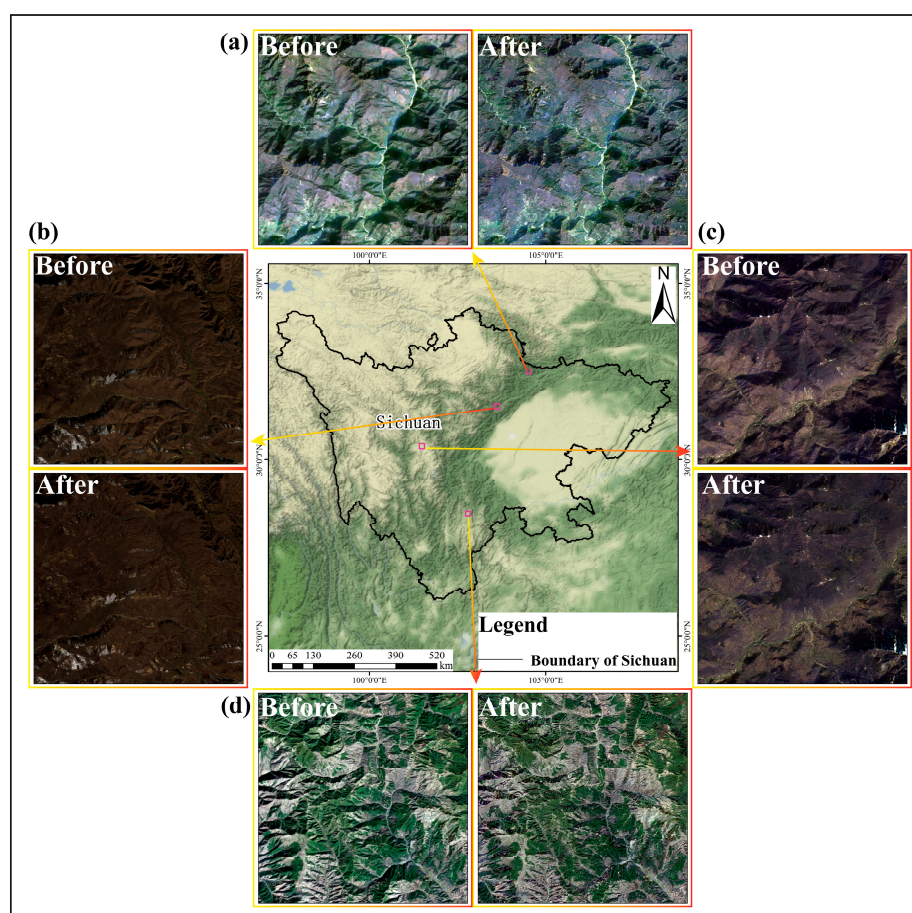


**Figure 3.** The comparison of topographic corrections for Landsat 8 OLI. (**a**). Before and after topographic corrections in region (**a**). (**b**). Before and after topographic corrections in region (**b**). (**c**). Before and after topographic corrections in region (**c**). (**d**). Before and after topographic corrections in region (**d**). The Sentinel-1 Ground Range Detected (GRD) data provided by GEE does not perform topographic correction due to artifacts on mountain slopes. In this study, we followed the method proposed by Mullissa et al. [65] and performed speckle filtering and topographic correction on the data in Google Earth Engine (Figure 4). The polarization was set as VV and VH, and the orbit was in the descending direction. The time period covered 1 January 2020 to 13 January 2020, capturing images during the dry season. The resulting image represents a snapshot of the dry season. To maintain data consistency, the spatial resolution of the Sentinel-1 data, which was originally 10 m, was resampled to 30 m when exporting the images using Google Earth Engine.
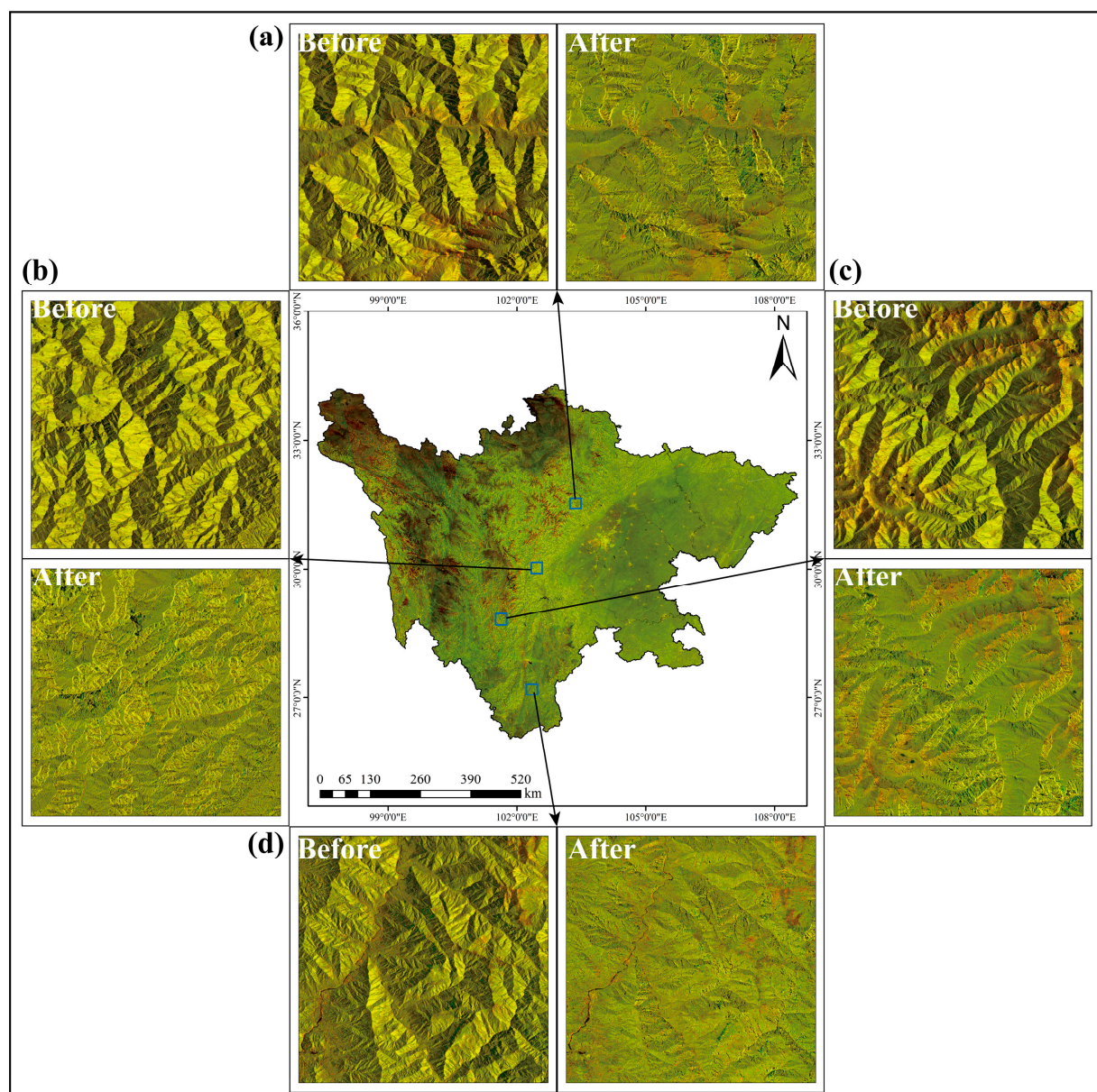
**Figure 4.** The comparison of topographic corrections for Sentinel 1B. (**a**). Before and after topographic corrections in region (**a**). (**b**). Before and after topographic corrections in region (**b**). (**c**). Before and after topographic corrections in region (**c**). (**d**). Before and after topographic corrections in region (**d**).

### 2.3.2. Environmental Variables Preprocessing

The precipitation data from 1 November 2019 to 31 March 2020 were synthesized into raster data with a spatial resolution of 30 m. The synthesized data included the average precipitation (Wpre), minimum precipitation (Wpre-min), and maximum (Wpre-max) precipitation during the dry season, as well as the average precipitation (Dpre), minimum precipitation (Dpre-min), and maximum precipitation (Dpre-max) during the wet season (from 1 May 2020 to 30 September 2020), all with a spatial resolution of 30 m. The differences between these variables were denoted as WDpre-min, WDpre, and WDpre-min (as shown in Appendix B Figure A1).

Similarly, the sunshine duration data from 1 November 2019 to 31 March 2020 were synthesized into raster data with a spatial resolution of 30 m using Kriging interpolation on ArcGIS into the average sunshine duration (Wssd), minimum sunshine duration (Wssd-min), and maximum (Wssd-max) sunshine duration in the wet season. The sunshine

duration data from 1 May 2020 to 30 September 2020 were synthesized into raster data with a spatial resolution of 30 m using Kriging interpolation on ArcGIS into the average sunshine duration (Dssd), minimum sunshine duration (Dssd-min), and maximum (Dssd-max) sunshine duration in the dry season with a spatial resolution of 30 m. Their difference was represented as WDssd-min, WDssd, and WDssd-min (as shown in Appendix B Figure A2).

Land surface temperature (LST) was obtained by inversion of the single window algorithm (SMW) proposed by Sofia et al. [58]. Specifically, we applied an inversion process to obtain three variables of LST: LST in the wet season (Wlst), LST in the dry season (Dlst), and their difference (DWlst) (as shown in Appendix B Figure A3). The entire process was implemented on the GEE cloud platform.

The NASADEM_HGT elevation data were used to calculate the slope and aspect for the terrain factor (as shown in Appendix B Figure A4).

### 2.3.3. Sample Datasets

The evergreen broad-leaved forests, a zonal vegetation, are widely distributed in Sichuan Province. To ensure uniform distribution of sample points, we visually interpreted the sampling points to supplement the sample data according to the characteristics, resulting in two types of sample plots: (i) field sampling plots and (ii) plots interpreted from images. We then established buffers around the recorded coordinates to balance the sample area of each layer, with the final number of samples shown in Table 2.

**Table 2.** The final number of samples.

| | Number of Field Sample Plot | Number of Interpreted Sample Plots | Number of Sample Plots | Buffer Distance | Sample Areas (m²) |
|---|---|---|---|---|---|
| Forests | 6866 | 0 | 6000 | 30 m | 16,964,586 |
| Non-forests | 0 | 1000 | 1000 | 70 m | 15,393,804 |
| Evergreen forests | 3049 | 0 | 3000 | 30 m | 8,482,309 |
| Non-evergreen forests | 3817 | 0 | 3000 | 30 m | 8,482,309 |
| Evergreen broad-leaved forests | 1389 | 111 | 1500 | 30 m | 4,241,150 |
| Evergreen non-broad-leaved forests | 1660 | 0 | 1500 | 30 m | 4,241,150 |
| HEBF | 1046 | 0 | 1000 | 30 m | 3,141,592 |
| SEBF | 343 | 157 | 500 | 45 m | 3,179,250 |

## 2.4. Hierarchy-Based Classifier

### 2.4.1. The Hierarchical Structure

Following the principle of "from top to bottom, from simple to complex, and from coarse to specific" [44], a hierarchical design was constructed, starting with the top layer (Layer 1) of "All land cover," which was split into two child nodes, "Forest" and "Non-forest". Next, the second layer focused on "Forest" while excluding "Non-forest".The parent node was split into two child nodes, "Evergreen forest" and "Non-evergreen forest". Similarly, the third layer focused on "Evergreen forest", while excluding "Non-evergreen forest". The parent node was further split into two child nodes, "Evergreen broad-leaved forest" and "Evergreen non-broad-leaved forest". Finally, the fourth layer was created, the "Evergreen broad-leaved forest" being split into "HEBF" and "SEBF". As the layers progressed from top to bottom, the splitting of the parent node to the next layer became increasingly intricate, necessitating more input features. Hence, the hierarchical structure illustrated in Figure 5 was designed based on the separability analysis of different vegetation types.
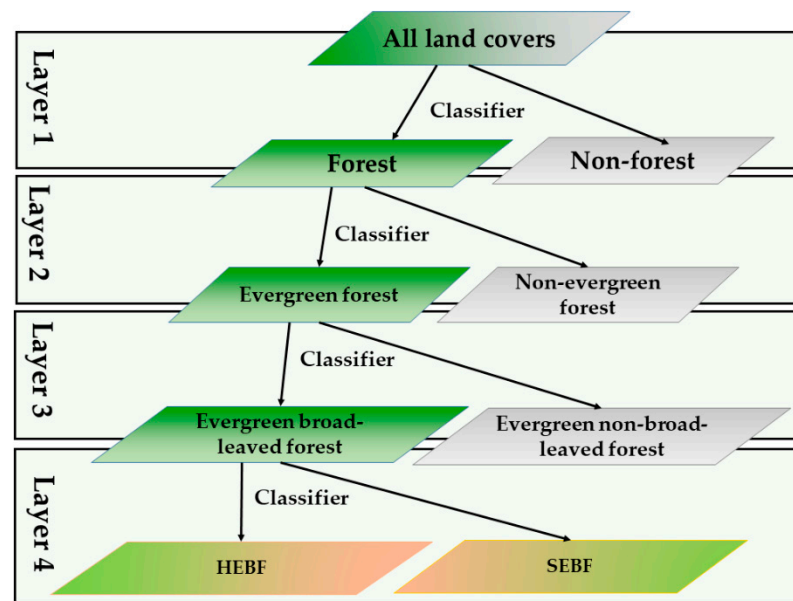
**Figure 5.** The hierarchical structure.

### 2.4.2. Features Selection

- Feature selection for extracting evergreen broad-leaved forests

Each layer in the proposed hierarchical structure has distinct features to differentiate specific vegetation properties. Figure 4 demonstrates that spectral information reflects the magnitude of electromagnetic wave energy reflected by ground objects, providing an intuitive representation of the characteristics. The top layer, represented by the parent node, encompasses all land cover types and can be easily divided into forest and non-forest due to their distinct spectral responses. We employed the normalized difference vegetation index (NDVI), the improved soil-atmosphere corrected vegetation index (EVI), and the forest discrimination index (FDI), which are commonly used to differentiate vegetation from non-vegetation [25]. The mathematical Equations (5)–(7) are as follows:

$$FDI = Nir - (Red + Green) \tag{5}$$

$$NDVI = \frac{Nir - Red}{Nir + Red} \tag{6}$$

$$EVI = 2.5 \frac{Nir - Red}{Nir + 6Red - 7.5Blue + 1} \tag{7}$$

The second layer was targeted to extract evergreen forests, which retain foliage year-round. Unlike non-evergreen forests, the NDVI and EVI values of evergreen forests show less variation over the year. Since the seasonal rhythm of vegetation is difficult to capture by single-date remote sensing images, the difference between NDVI and EVI between the dry and wet seasons serves as an effective means to identify evergreen forests.

The third parent node, "Evergreen forest," encompasses both broad-leaved and evergreen coniferous forests. Spectrally, these forest types exhibit similarities, posing challenges in their differentiation based on spectral features alone. However, their textural features in remote sensing images display notable distinctions [63]. Haralik et al. [66,67] proposed 14 texture features using the Grey-Level Co-occurrence Matrix (GLCM). Mean, variance, homogeneity, contrast, dissimilarity, entropy, second moment, and correlation are texture features often used to automatically classify vegetation types. Principal Component Analysis (PCA) [68] is often employed to reduce the dimensionality of the 16 texture feature information to three principal component information, namely PC1, PC2, and PC3, to miti-

gate data redundancy. Hence, texture features were added to the third layer to distinguish evergreen broad-leaved forests and evergreen non-broad-leaved forests on remote sensing images, thus obtaining the evergreen broad-leaved forests map.

- Feature selection for classifying the HEBF and SEBF

Based on field surveys, we concluded the environment conditions and canopy appearance differences between HEBF and SEBF. The HEBF predominantly occurs in the basin and low-middle mountains on the edge, featuring a warm and humid climate, abundant clouds and fog, high humidity, and less sunshine. The average annual temperature is 14–18 °C, and the precipitation is evenly distributed throughout the year, averaging annual precipitation of 900–1000 mm. The average monthly temperature in the dry season is 5–8 °C, and the average monthly temperature in the wet season is 15–20 °C, without a clear demarcation between wet and dry seasons. The HEBF exhibits a diverse community composition with a variety of dominant species, and its understory is rich in plants and characterized by heat and humidity-loving plants. The canopy of HEBF is deep green, and the hierarchical structure is complex.

The climate of the southwestern mountainous region, where SEBF occurs, is characterized by warm winters and cool summers, featuring well-defined wet and dry seasons, limited cloud cover, and ample sunshine. The annual mean temperature ranges from 12 to 17 °C, and the annual precipitation ranges from 800 to 1050 mm, with 95% of the total precipitation occurring during the wet season and the average temperature during the dry season being 4–9.5 °C with less precipitation. The total sunshine hours per year is approximately 2400 h, accounting for 55% of the total sunshine hours. The SEBF community displays relatively low species diversity, with a sparse understory of trees, primarily comprising drought-tolerant grasses and seedlings. The community appears pale yellow-green in color, with a simple stratification and distinct seasonal canopy.

In summary, the key to distinguishing HEBF and SEBF is the differences in canopy appearance and structure during the dry season. Therefore, we employed vegetation moisture indices, Tasseled Cap Transformation (TCT), and other spectral band changes to characterize canopy information in the fourth layer to differentiate between the two types of forests. The canopy moisture index integrates the total water column content by combining the absorption characteristics of water in the near-infrared and short-wave infrared ranges and the penetration of light in the near-infrared range. Several vegetation indices were selected to represent the water content of the vegetation canopy, including the Ratio Vegetation Index (RVI) [69], the Normalized Infrared Index (NDII), and the Moisture Stress Index (MSI) [70]. The mathematical equations for these indices are given by Equations (8)–(10). Tasseled Cap Transformation (TCT) [27] transforms vegetation and soil information onto a plane in multi-dimensional space, where the temporal trajectory of vegetation growth (spectral graph) and the soil brightness axis are perpendicular to each other. TCT enables us to represent the "brightness", "greenness", and "yellowness" of vegetation through TC1, TC2, and TC3, respectively. These indices reflect information about soil and rock, vegetation, and water content in soil and vegetation. The change matrix of the tasseled-cap transformation of the Landsat 8 OLI image was used to analyze the differences between HEBF and SEBF.

The mathematical Equations (8)–(10) are as follows:

$$\text{RVI} = \frac{\text{Nir}}{\text{Red}} \tag{8}$$

$$\text{NDII} = \frac{\text{Nir} - \text{Swir1}}{\text{Nir} + \text{Swir1}} \tag{9}$$

$$\text{MSI} = \frac{\text{Swir1}}{\text{Nir}} \tag{10}$$

Furthermore, Sentinel-1 is a short-wavelength Synthetic Aperture Radar (SAR) that interacts with the upper part of the vegetation canopy to retrieve biophysical vegetation parameters. The vegetation structure information derived from Sentinel-1 SAR data complements the optical data. We performed SCS + C topography correction and Peron–Malik speckle filtering for the C-band SAR (VV and VH) data. The resampled data were matched to the Landsat 8 data, which have a spatial resolution of 30 m and were added as a layer for features classification.

Vegetation and environmental factors, such as climate, geomorphology, and moisture, especially the dominant factors, exhibit a strong correlation and relative consistency in spatial distribution [37,38]. At a regional scale, zonal climate conditions are the dominant factors determining the spatial pattern of vegetation. In mountainous areas, vertical zonation is a prominent characteristic of vegetation. From the foothills to the mountain tops, there are significant differences in climatic conditions, and the composition of vegetation changes markedly with altitude, slope direction, and slope [71,72]. Different environmental conditions give rise to distinct subtypes of the same vegetation type. Thus, environmental variables were incorporated to enhance the classification accuracy of HEBF and SEBF. Six types of environmental variables (precipitation, sunshine duration, surface temperature (LST), elevation, slope, and aspect) were selected to explore the influence of environmental factors on the spatial differentiation of evergreen broad-leaved forest from three aspects: heat, moisture, and topography. As HEBF and SEBF also exhibit seasonal differences in precipitation, sunshine duration, and surface temperature (LST), the maximum, minimum, and mean values of these three variables were calculated for both the dry season and wet season. Therefore, it was necessary to prioritize the selection of environmental variables that contributed significantly to the classification of HEBF and SEBF to avoid data redundancy. Traditional statistical methods and models, such as regression and correlation analysis, have been widely used to determine the contribution of driving factors to spatial vegetation differentiation [73,74]. Traditional models often ignore multicollinearity and spatial relationships among driving factors. Geodetector, a powerful tool that can detect spatial heterogeneity, offers a notable advantage by revealing the detect the relationship between driving factors and geographical phenomena without any linear assumptions. Thereby revealing the driving role of variables in geographical phenomena. Therefore, it is widely used for quantitative analysis of environmental factors driving vegetation spatial differentiation. Geodetector includes four detectors: Coverage Detector, Interaction Detector, General Detector, and Intervention Detector. The Coverage Detector examines the influence of each factor on the variation in geographic phenomena, indicating the independent contribution of each factor. Its q statistic can quantify the contribution of an individual driving factor and the interaction strength between two detection factors. The value ranges from 0 to 1, representing the relative size of the contribution. A higher q value indicates greater explanatory power of the variable for other variables and a stronger influence of its change on other variables. The Interaction Detector is used to analyze the influence degree of the interaction between factors on the variation of geographic phenomena, that is, the mutual influence between each factor [75–77]. In this study, the Coverage Detector and Interaction Detector were used to assess the explanatory power of environmental variables in the spatial differentiation of evergreen broad-leaved forests, and environmental variables with high explanatory power were selected as inputs for the classifier.

### 2.5. Classification Scheme Device

This study aimed to classify two types of vegetation, HEBF and SEBF, by considering their characteristic combinations across different layers. To achieve this, we employed three well-known classifiers, namely RF, SVM, and GBT, to identify the classifier with the highest accuracy for each layer. Among them, both RF and GBT employ 100 initial decision trees. To evaluate the performance of our models and identify overfitting or underfitting problems, we employed 10-fold cross-validation in each layer. This involved dividing our dataset into 10 parts, using one part for validation while training the model on the remaining nine parts.

We repeated this process 10 times and selected the classifier parameters with the highest training accuracy from the selected fold for classifying the entire region. All classification experiments were conducted using the Google Earth Engine (GEE) platform. For the fourth layer, we interpolated the environmental variables data using ArcGIS and imported it into GEE for classification. The classification scheme is summarized in Table 3.

**Table 3.** Descriptions of the classification schemes.

| Layer | Classifier | Features Group |
|---|---|---|
| Layer 1 | RF | |
| | SVM | Spectral features |
| | GTB | |
| Layer 2 | RF | Spectral features |
| | SVM | Temporal features |
| | GTB | |
| Layer 3 | RF | Spectral features |
| | SVM | Temporal features |
| | GTB | Sentinel 1 features |
| Layer 4 | RF | Spectral features |
| | SVM | Temporal features |
| | | Sentinel 1 features |
| | GTB | Environment variables |

*2.6. Accuracy Assessment*

To verify the accuracy of the hierarchy-based classifier, we calculated the User's Accuracy (UA), Producers Accuracy (PA), Overall Accuracy (OA), and Kappa coefficient. These indices are calculated based on the confusion matrix, which represents the accuracy evaluation with an n column and n row. Each column represents the predicted category, and the total number of each column represents the number of data predicted to be in that category; each row represents the true attribution category of the data, and the total number of data in each row represents the number of data instances in that category. The value in each column represents the number of real data predicted to be in that category. Users' accuracy reflects misclassification error, Producers' accuracy reflects omission error, and OA and Kappa coefficient can accurately reflect the overall classification accuracy. The formulas are as Equations (11)–(14):

$$\mathrm{PA} = X_{ij}/X_{+i} \tag{11}$$

$$\mathrm{UA} = X_{ij}/X_{i-} \tag{12}$$

$$\mathrm{OA} = \frac{\sum_{i=1}^{n} X_{ij}}{N} \tag{13}$$

$$\mathrm{Kappa} = \frac{N \cdot \sum_{i=1}^{n} X_{ij} - \sum_{i=1}^{n} (X_{i+} + X_{+i})}{N^2 - \sum_{i=1}^{n} (X_{i+} + X_{+i})} \tag{14}$$

where $n$ is the number of rows, $X_{ij}$ is the number of elements in row $i$ and column $j$, $X_{+i}$ is the sum of columns, $X_{+i}$ is the sum of rows, and $N$ is the sum of all elements.

The hierarchy-based classifier has four layers, and each layer will have the accuracy of PA, UA, OA, and Kappa coefficient of three classifiers. The result with the best performance in each layer is selected as the parent node of the lower layer to improve classification accuracy. Each layer also had its error; thus, the accuracy of extracting evergreen broad-leaved forest using the hierarchy-based classifier was determined by multiplying the best accuracy selected by the forest layer, evergreen forest layer, and evergreen broad-leaved forest layer. Consequently, the resulting accuracy of the HEBF and SEBF classification

obtained using the hierarchy-based classifier was the accuracy of extracting evergreen broad-leaved forest multiplied by the accuracy of Layer 4.

## 3. Results

### 3.1. Extraction Results of the Evergreen Broad-Leaved Forest

We evaluated the accuracy of the three classifiers in each layer and selected the best-performing classifier for the subsequent classification experiment. The final classification accuracy was obtained by multiplying the best classification accuracies of each layer. Table 4 below shows the classification accuracy for each layer.

**Table 4.** The extraction accuracy of the evergreen broad-leaved forest.

| | Layers | Classifier | Optimal Parameters | PA | UA | OA | Kappa |
|---|---|---|---|---|---|---|---|
| Layer 1 | Forest | RF | Ntree = 85 | 97.92% | 97.92% | 97.98% | 0.96 |
| | Non-forest | | Kfold = 3 | 98.04% | 98.04% | | |
| | Forest | SVM | Kfold = 3 | 99.98% | 90.57% | 94.95% | 0.89 |
| | Non-forest | | | 90.20% | 99.98% | | |
| | Forest | GTB | Ntree = 10 | 95.83% | 97.87% | 96.97% | 0.94 |
| | Non-forest | | Kfold = 6 | 96.15% | 96.15% | | |
| Layer 2 | Evergreen forest | RF | Ntree = 30 | 93.48% | 95.56% | 93.51% | 0.87 |
| | Non-evergreen forest | | Kfold = 3 | 93.55% | 90.63% | | |
| | Evergreen forest | SVM | Kfold = 9 | 62.16% | 82.14% | 75.32% | 0.50 |
| | Non-evergreen forest | | | 87.50% | 71.43% | | |
| | Evergreen forest | GTB | Ntree = 60 | 91.38% | 96.36% | 91.25% | 0.79 |
| | Non-evergreen forest | | Kfold = 10 | 90.91% | 80.00% | | |
| Layer 3 | Evergreen broad-leaved forest | RF | Ntree = 30 | 98.55% | 97.14% | 97.60% | 0.95 |
| | Evergreen non-broad-leaved forest | | Kfold = 7 | 98.18% | 96.43% | | |
| | Evergreen broad-leaved forest | SVM | Kfold = 3 | 98.04% | 90.91% | 94.92% | 0.90 |
| | Evergreen non-broad-leaved forest | | | 92.54% | 98.41% | | |
| | Evergreen broad-leaved forest | GTB | Ntree = 50 | 98.15% | 94.64% | 96.61% | 0.93 |
| | Evergreen non-broad-leaved forest | | Kfold = 7 | 95.31% | 98.39% | | |
| Extraction accuracy of the evergreen broad-leaved forest using a hierarchy-based classifier | | | | 90.21% | 90.90% | 89.42% | 0.79 |

Based on the table above, it is evident that RF achieves the highest performance in each layer, whereas SVM exhibits the lowest performance. Consequently, we selected the classification results of RF from each layer to be employed in the subsequent layer's classification experiment. The classification accuracy of the hierarchy-based classifier is ultimately determined by multiplying the highest classification accuracies from each layer. The overall accuracy (OA) and Kappa accuracy of the final classification results are 89.42% and 0.79, respectively.

Figure 6 illustrates the results of the three classifiers employed in the initial layer for forest classification.

Based on Figure 6 above, it is evident that the classification results of RF and GTB exhibit similarity with a small accuracy difference, while SVM demonstrates a significantly higher number of misclassifications. Furthermore, from the table, it can be observed that the user's accuracy (UA) of SVM is lower than the producer's accuracy (PA), indicating a significant misclassification issue.

Figure 7 depicts the results of the three classifiers employed in the second layer for classifying evergreen forests.
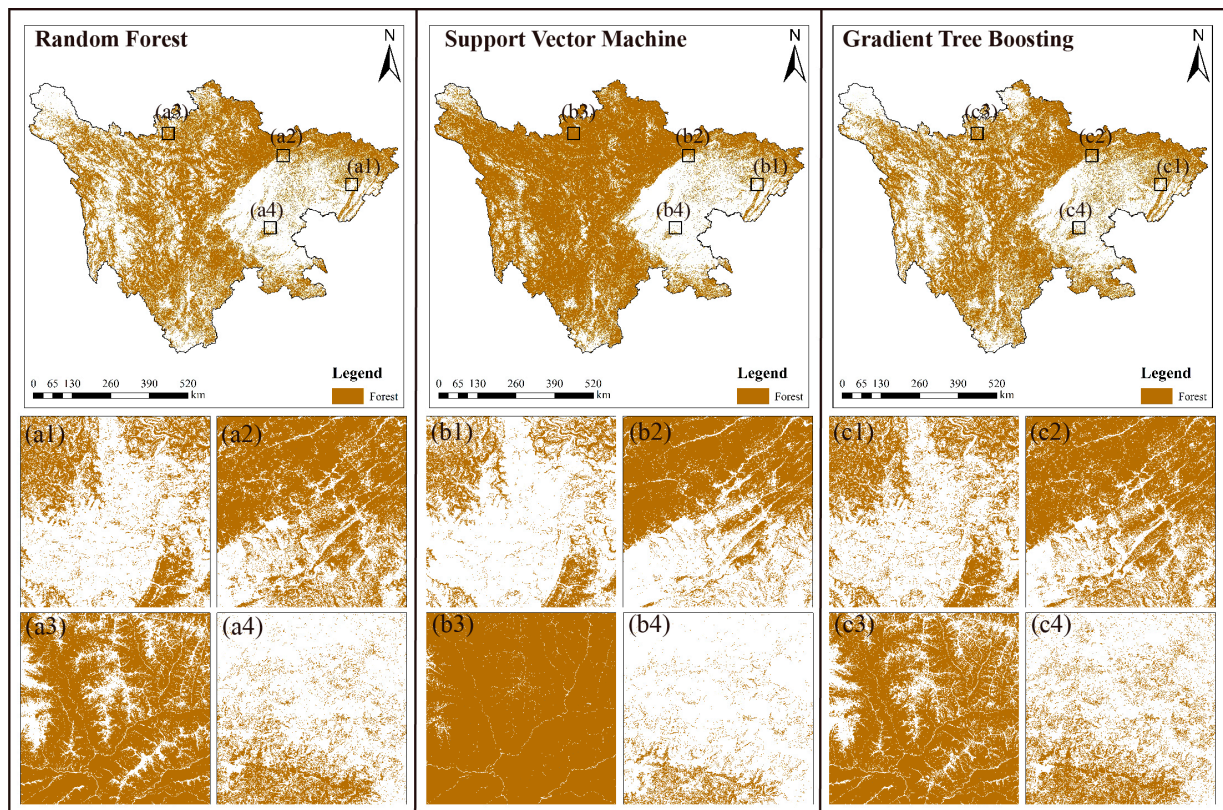
**Figure 6.** The results of the forest map. (**a1**–**a4**). Results of Random Forest classification for forest in four regions. (**b1**–**b4**). Results of Support Vector Machine classification for in four regions. (**c1**–**c4**). Results of Gradient Tree Boosting classification for forest in four regions.
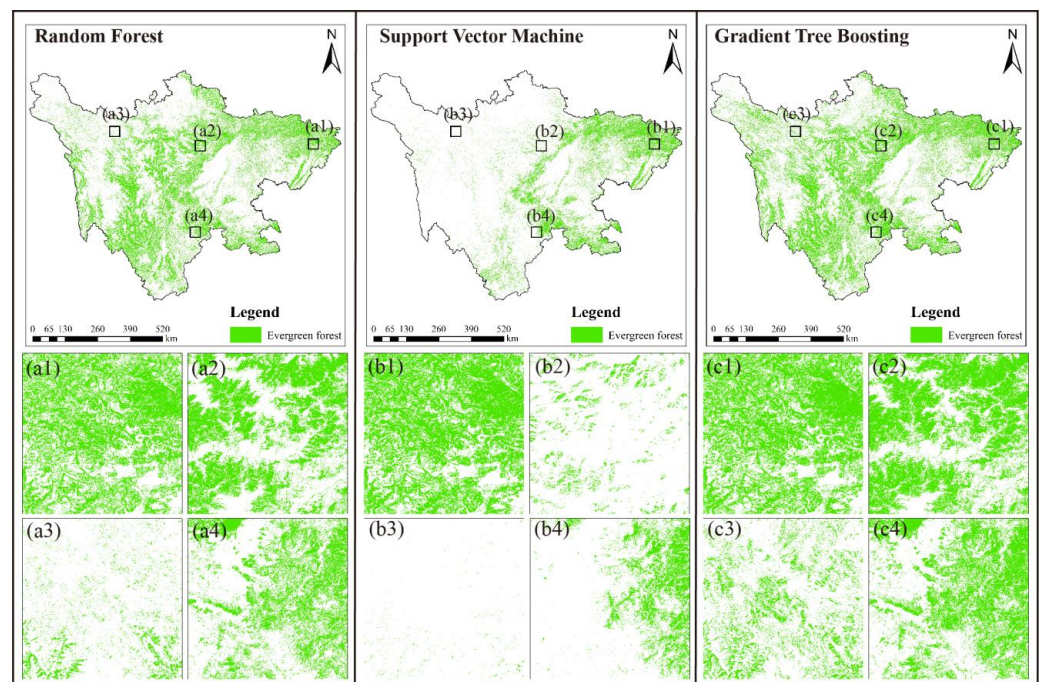


**Figure 7.** The results of the evergreen forest map. (**a1**–**a4**). Results of Random Forest classification for evergreen forest in four regions. (**b1**–**b4**). Results of Support Vector Machine classification for evergreen forest in four regions. (**c1**–**c4**). Results of Gradient Tree Boosting classification for evergreen forest in four regions.

Based on Figure 7 above, it can be observed that while the UA of GTB is slightly higher than that of RF, RF demonstrates the highest PA, OA, and Kappa accuracy. Consequently, we have chosen RF's classification results as the parent node for the lower-level classification. Additionally, the figure highlights significant omissions in SVM, leading to a lower PA compared to other methods.

The results of the three classifiers utilized in the third layer for evergreen broad-leaved forest classification are illustrated in Figure 8:
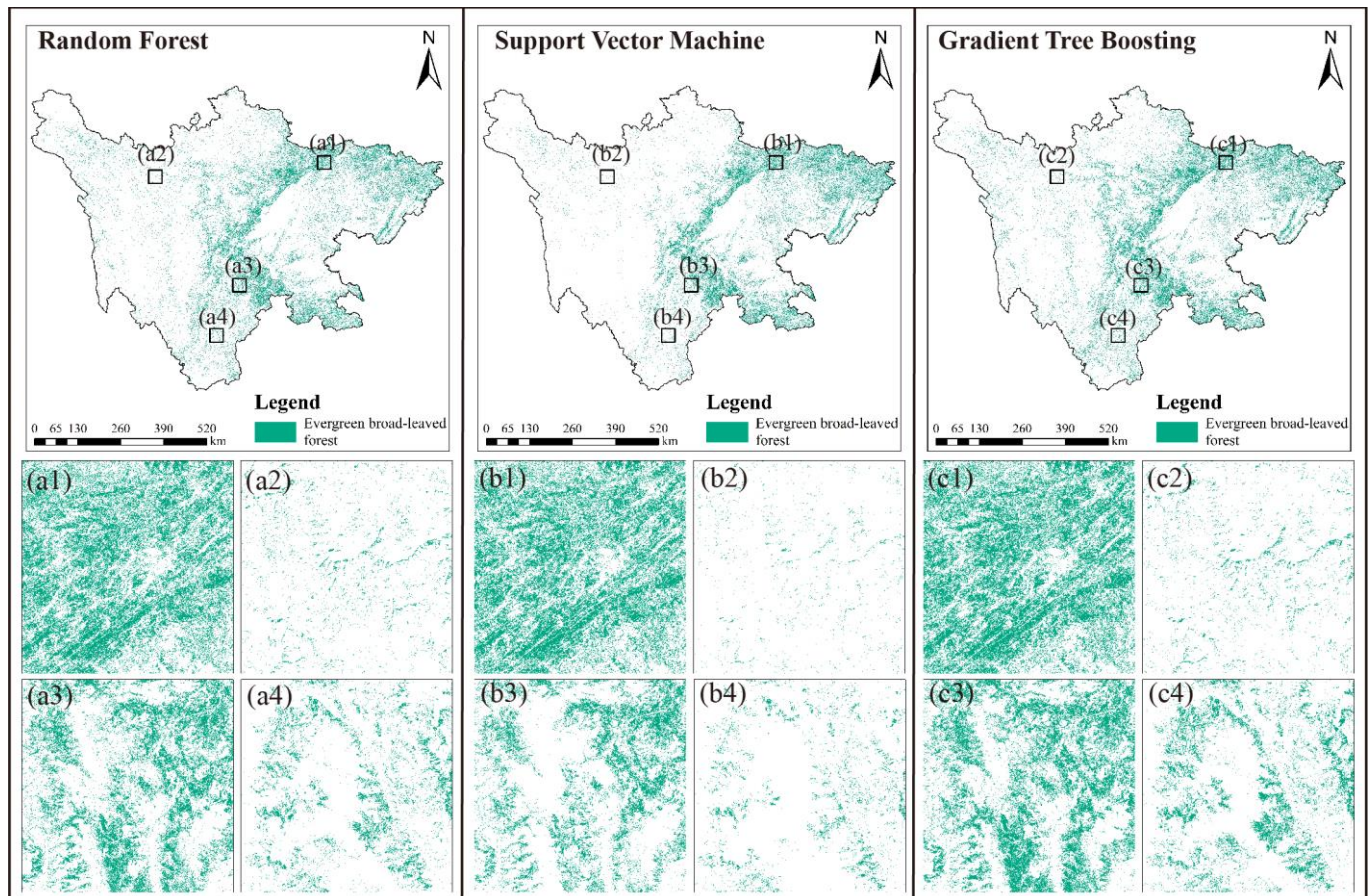


**Figure 8.** The results of the evergreen broad-leaved forest map.(**a1**–**a4**). Results of Random Forest classification for evergreen broad-leaved forest in four regions. (**b1**–**b4**). Results of Support Vector Machine classification for evergreen broad-leaved forest in four regions. (**c1**–**c4**). Results of Gradient Tree Boosting classification for evergreen broad-leaved forest in four regions.Based on the above results, RF exhibits the highest precision regarding PA, UA, OA, and Kappa, making it the preferred classification result for the lower-level HEBF and SEBF classifications. As shown in Figure 8, SVM has a significant under-classification issue, and although GTB's classification accuracy is considerable, it is still inferior to that of RF. Ultimately, we obtained the accuracy of extracting evergreen broad-leaved forest by multiplying the RF accuracy of each layer, which are PA at 90.23%, UA at 89.87%, OA at 89.42%, and Kappa at 0.79.
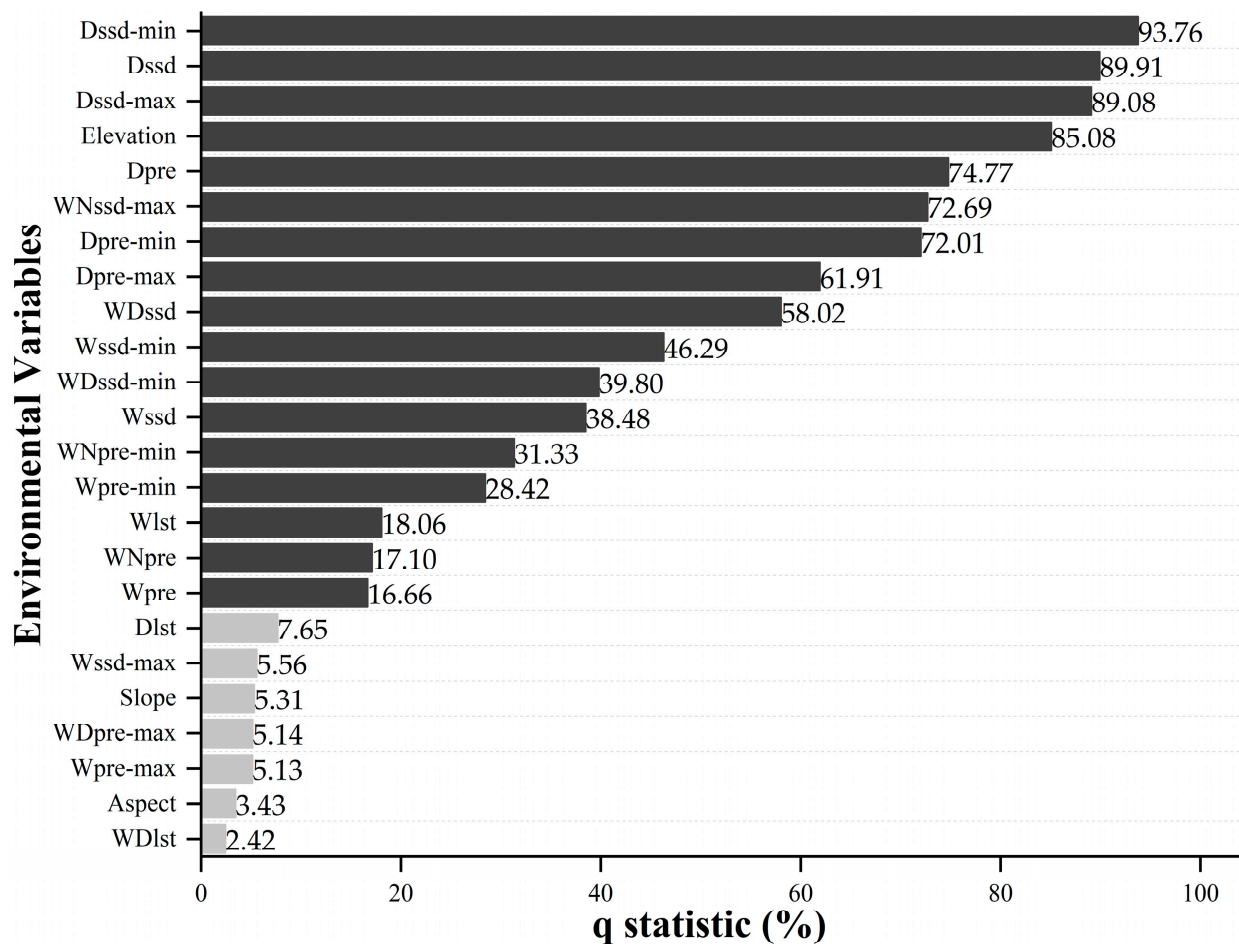
### 3.2. Filtering of Environmental Variables

As Geodetector requires categorical input variables, continuous variables need to be discretized. Using the natural interruption point grading method proposed by Jinfeng Wang et al. [66,67], the 24 environmental variables were graded based on data discretization and a priori knowledge. The classes are presented in Table 5.

**Table 5.** Numbers of ratings for environmental variables.

| Environmental Variables | Classes | Environmental Variables | Classes |
|---|---|---|---|
| Wpre-min | 5 | Wssd-min | 10 |
| Wpre | 5 | Wssd | 10 |
| Wpre-max | 5 | Wssd-max | 10 |
| Dpre-min | 5 | Dssd-min | 8 |
| Dpre | 5 | Dssd | 8 |
| Dpre-max | 5 | Dssd-max | 8 |
| WDpre-min | 6 | WDssd-min | 10 |
| WDpre | 8 | WDssd | 10 |
| WDpre-max | 6 | WDssd-max | 10 |
| Elevation | 8 | Wlst | 8 |
| Slope | 8 | Dlst | 8 |
| Aspect | 9 | WDlst | 8 |

The q-value of the Geodetector's Factor detector (Figure 9) shows the driving effect of each factor on the spatial differentiation of the HEBF and SEBF. The maximum q statistic was for Dssd-min (0.938), while Dssd and Dssd-max were 0.899 and 0.891, respectively, indicating that sunshine duration in the dry season contributes the most to the spatial differentiation of the HEBF and SEBF; topographically, the contribution of elevation (0.851) is also significantly more extensive than that of slope (0.053) and aspect (0.0343); additionally, the q statistic of dry season's precipitation is 0.748, 0.720, and 0.619, respectively, indicating their strong contribution.



**Figure 9.** The q statistic of the Factor_detector.(q statistic of environmental variables greater than 10% for are depicted in black, while q statistic less than 10% are depicted in gray).

The contribution of environmental variables to the spatial differentiation of HEBF and SEBF in the dry season is significantly greater than that in the wet season, especially the contribution of sunshine duration and precipitation in the dry season, which are both above 0.6. The contributions of LST were low. In summary, dry season sunshine duration and precipitation and elevation are the main driving factors of spatial differentiation in the HEBF and the SEBF. Therefore, we selected the environmental variables with a contribution rate greater than 50% and added them to the classification of HEBF and SEBF. These variables include Dssd-min, Dssd, Dssd-max, elevation, Dpre, WNssd-max, Dpre-min, Dpre-max, and WDssd.

In addition, interactions between environmental variables and the effects were non-linearly enhanced. The most substantial explanatory power of the interactions (>85%) was in the synergistic effect of elevation and dry season sunshine duration with other drivers; this was followed by the interaction of non-growing season precipitation with the remaining factors, with the explanation power above 62%.

*3.3. Classification Results of the HEBF and SEBF*

Finally, we obtained the classification accuracy of HEBF and SEBF using the hierarchy-based classifier in combination with environmental variables, as shown in Table 6 below:

**Table 6.** Classification accuracy of the HEBF and SEBF.

|  |  | Classifier | Optimal Parameters | PA | UA | OA | Kappa |
|---|---|---|---|---|---|---|---|
| Layer 4's accuracy | HEBF | RF | Ntree = 55 | 97.22% | 99.98% | 98.31% | 0.96 |
|  | SEBF |  | Kfold = 5 | 99.99% | 95.83% |  |  |
|  | HEBF | SVM | Kfold = 7 | 99.98% | 94.87% | 96.72% | 0.93 |
|  | SEBF |  |  | 91.67% | 99.98% |  |  |
|  | HEBF | GTB | Ntree = 50 | 99.97% | 92.50% | 95.09% | 0.89 |
|  | SEBF |  | Kfold = 1 | 87.50% | 99.98% |  |  |
| Hierarchy-based classifier's accuracy | HEBF |  |  | 87.70% | 90.88% | 87.91% | 0.76 |
|  | SEBF |  |  | 90.20% | 87.11% |  |  |

In the fourth layer, RF still demonstrated the best accuracy, so we multiplied the accuracy obtained in the fourth layer with the accuracy of extracting evergreen broad-leaved forest obtained in Section 3.1 to obtain the classification accuracy of HEBF and SEBF based on the hierarchy-based classifier as OA 87.91% and Kappa 0.76. The following Figure 10 shows the final result of classifying HEBF and SEBF.

The evergreen broad-leaved forests are widely distributed in Sichuan, particularly in the southeastern region of the northern Daba Mountains, Micang Mountains, Pingwu, Beichuan, Maowen, Wenchuan, Luding, Jiulong, and Muli lines. The HEBF is primarily found in the mountainous areas on the southern edge of the Sichuan Basin, the bottom of the mountainous basins in the western part of the basin (square hills and parallel valleys), and the low-elevation areas on the southern slopes of the Daba Mountains and Micang Mountains, the central mountain areas on the eastern edge of the Sichuan Basin, or the tops of the ridges of low mountains. In contrast, the SHEB is mainly distributed in the southwestern mountains and, to a lesser extent, in the western Sichuan Plateau.
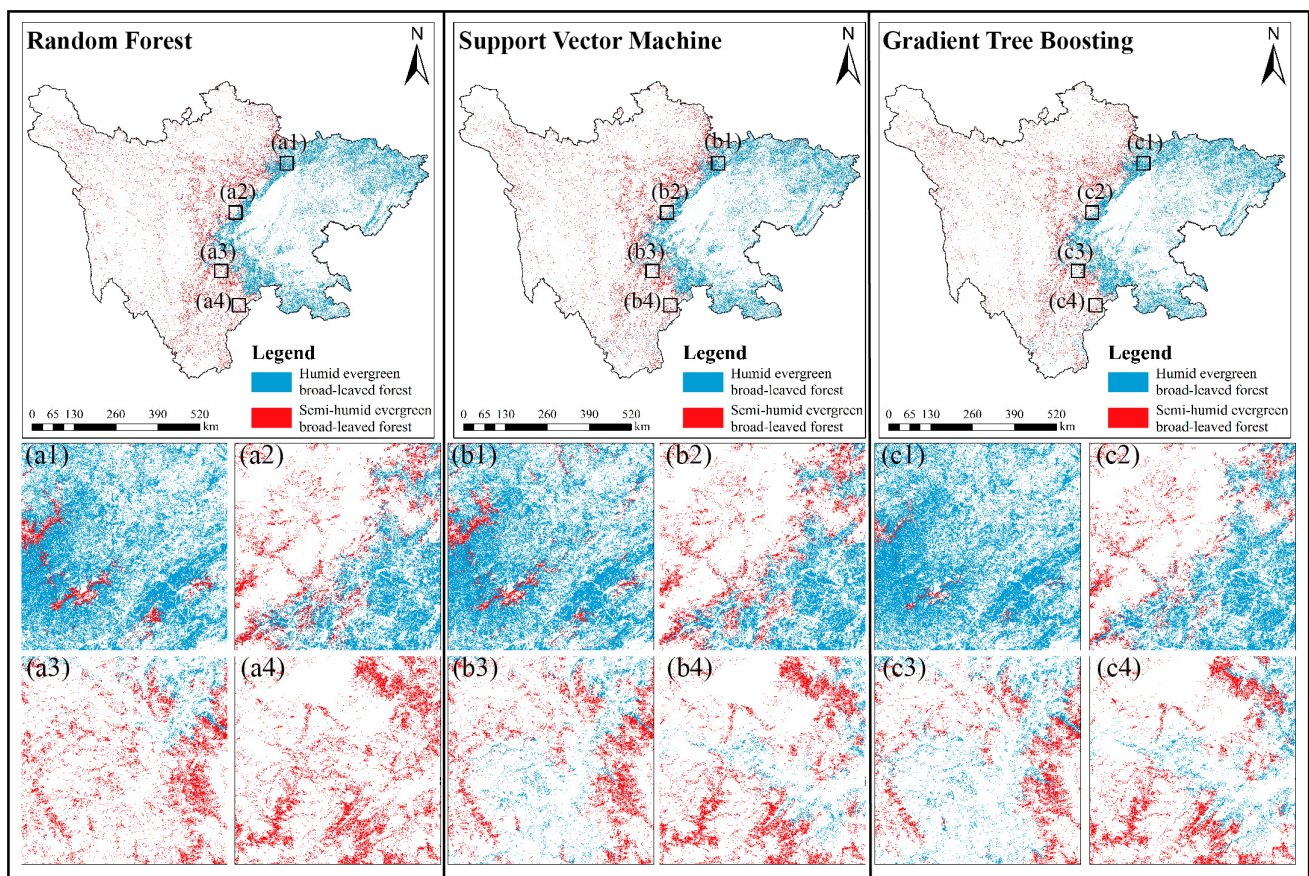
**Figure 10.** The results of the HEBF and SEBF map. (**a1**–**a4**). Results of Random Forest classification for HEBF and SEBF in four regions. (**b1**–**b4**). Results of Support Vector Machine classification for HEBF and SEBF in four regions. (**c1**–**c4**). Results of Gradient Tree Boosting classification for HEBF and SEBF in four regions.Figure 10 clearly shows that all three classifiers can clearly distinguish a noticeable boundary between HEBF and SEBF. However, there are still differences on either side of the boundary. RF still performs the best in classifying HEBF and SEBF, particularly with greater accuracy in SEBF classification. In contrast, SVM and GTB tend to misclassify SEBF as HEBF at the same location.

## 4. Discussion

### 4.1. Sensitivity Analysis of Classification Accuracy

Despite the incorporation of DEM for terrain correction in Landsat 8 Collection 2 data, it is important to distinguish between terrain correction and topographic correction. Terrain correction primarily addresses the non-uniformity of brightness and radiance in the image, whereas topographic correction specifically aims to mitigate the impact of terrain on illumination and reflectance. Hence, terrain correction alone does not account for the same factors as topographic correction [50]. In mountainous environments, the pronounced influence of terrain on reflectance, attributed to illumination effects and cast shadows, introduces errors in land cover classification. Recent studies have emphasized the necessity of applying topographic correction when analyzing Landsat satellite imagery in mountainous regions, particularly for accurate vegetation classification. Despite its exclusion from the standard data preprocessing chain, such as Landsat Analysis Ready data, the implementation of topographic correction is recommended to ensure robust and reliable results [52,54,78]. In this study, SCS + C was used to perform topographic correction on remote sensing images of large areas to improve the accuracy of vegetation classification. To assess the effectiveness of topographic correction on classification accuracy, the same samples and a hierarchy-based classifier were employed to compare the classification results before

and after topographic correction. The classification accuracy without SCS + C topographic correction is shown in Table 7:

**Table 7.** The Classification accuracy without SCS + C topographic correction.

| Layer | | Classifier | Optimal Parameters | PA | UA | OA | Kappa |
|---|---|---|---|---|---|---|---|
| Layer 1 | Forest<br>Non-forest | RF | Ntree = 50<br>Kfold = 2 | 94.83%<br>85.37% | 90.16%<br>92.11% | 90.91% | 0.81 |
| Layer 2 | Evergreen forest<br>Non-evergreen forest | RF | Ntree = 30<br>Kfold = 10 | 90.91%<br>81.48% | 90.91%<br>81.48% | 87.80% | 0.72 |
| Layer 3 | Evergreen broad-leaved forest<br>Evergreen non-broad-leaved forest | RF | Ntree = 55<br><br>Kfold = 9 | 87.01%<br><br>93.7% | 95.71%<br><br>81.82% | 89.60% | 0.78 |
| Layer 4 | HEBF<br>SEBF | RF | Ntree = 60<br>Kfold = 8 | 97.22%<br>88.00% | 92.11%<br>95.65% | 93.44% | 0.86 |
| Hierarchical accuracy | HEBF<br>SEBF | | | 72.93%<br>66.01% | 72.26%<br>75.04% | 66.83% | 0.40 |

The results in Table 7 indicate that topographic correction improved the accuracy of mountain vegetation classification, particularly in the forest layer. The topographic correction image exhibited a 7.74% higher PA value and a 3.09% higher UA value than the original image. This implies that the topographic correction effectively avoided misclassification and omission of forest types. The accuracy of each subsequent layer with topographic correction was better than that without topographic correction, likely due to the lower accuracy of the forest layer, which affected the subsequent classification results and caused a larger error accumulation in the final pass through the hierarchical classifier. The implementation of topographic correction in this study area yielded improved classification results of the two vegetation subtypes, consistent with the findings of previous studies [53].

This study employs the Single-Window Method (SWM) to retrieve land surface temperature, taking into account the influence of forest microclimate. In general, near-surface temperature data for environmental variables are commonly derived from meteorological station observations. However, it is essential to consider the impact of forest microclimates on temperature measurements [79]. Spatial interpolation techniques are often employed to estimate temperature values in a continuous raster format based on discrete meteorological station data. Nevertheless, it is crucial to acknowledge the influence of vegetation on temperature and humidity dynamics, which are regulated by processes such as photosynthesis, transpiration, and evapotranspiration. These biological processes lead to significant temperature variations between vegetated and non-vegetated areas [80]. Additionally, it is important to note that weather stations are typically situated in open and flat regions, which may not accurately represent the canopy temperature of forested areas. Precipitation and solar radiation intensity are less susceptible to forest microclimates and can be reliably obtained from meteorological data sources. These variables are often measured at weather stations and provide valuable information on local climatic conditions. Therefore, when analyzing precipitation and solar radiation intensity, utilizing meteorological data is a suitable approach to capture the spatial and temporal variations in these parameters. In summary, while meteorological station observations are commonly used for near-surface temperature data, the influence of vegetation and the limitations of weather station locations should be considered. Conversely, precipitation and solar radiation intensity can be effectively derived from meteorological data sources due to their relatively lower sensitivity to forest microclimates. These considerations ensure the accurate representation of environmental variables in studies focused on forest ecosystems and their interactions with climate.

Conversely, a hierarchy-based classifier was proposed to extract the evergreen broad-leaved forest and classify its vegetation subtypes, namely HEBF and SEBF. To evaluate the performance of the proposed method, Random Forest (RF) was employed to directly classify the HEBF and SEBF vegetation subtypes from images of the entire study area after SCS + C topographic correction. The experiment maintained consistent settings, feature variables, and samples. Table 8 presents the classification accuracy achieved using Random Forest.

**Table 8.** The classification accuracy using random forest.

| Layer | Training Parameters | PA | UA | OA | Kappa |
|---|---|---|---|---|---|
| HEBF | Ntree = 50 | 78.57% | 89.19% | 84.88% | 0.70 |
| SEBF | Kfold = 7 | 90.91% | 81.63% | | |

Compared to the direct use of RF for HEBF and SEBF classification, the use of hierarchy-based classifiers improved the OA and Kappa by 3.02% and 6.57%, respectively. The results in the table show that the accuracy of the hierarchy-based classifier was superior to that of the direct use of the classifier in extracting broadleaf evergreen forest in a complex background, resulting in more precise classification results for HEBF and SEBF. Therefore, the proposed method effectively extracts vegetation types in a larger and more complex background based on the vegetation characteristics, despite the hierarchy-based classifier accumulating the error of each layer, which makes the vegetation classification of complex mountainous areas more accurate. After all, in previous global or national remote sensing classification products, such as GLC_FCS30, MCD12Q1, and UMD Land Cover, the distribution range of its evergreen broad-leaved forests in Sichuan Province varies relatively widely.

### 4.2. Analysis of Spatial Patterns of Evergreen Broad-Leaved Forest in Sichuan Province

The evergreen broad-leaved forests in Sichuan Province are an important part of the subtropical evergreen broad-leaved forest in China. In this study, we quickly obtained the spatial distribution range of the evergreen broad-leaved forest in Sichuan Province by remote sensing technology and quantitatively classified the HEBF and SEBF. This result was verified with accuracy using field survey data and coincided with the ecological niche predictions of HEBF and SEBF by Liu Ying et al. [81] using MaxEnt. We found that the distribution limits of the HEBF and the SEBF vary greatly not only horizontally but also vertically, with the upper elevation limit of the SEBF distribution at 3000 m and the HEBF distribution's upper elevation limit approximately below 2000 m. The distribution boundaries between the HEBF and the SEBF are influenced by the respective landscape types and moisture and heat in the dry season.

The HEBF has a higher species richness and a rich understory populated by heat and humidity-loving plants. In contrast, the SEBF has a lower species richness, mainly *Cyclobalanopsis gracilis, Castanopsis delavayi, Lithocarpus cleis-tocarpus*, and is almost a single. The understory is dominated by drought-tolerant grasses and seedlings. This evergreen broadleaf forest has similar distribution differences to Yunnan Province, while Yunnan and Sichuan Province have similar vegetation distribution and environment in general. According to the vegetation geography of evergreen broadleaf forest in Yunnan Province by researcher Zhu Hua [82], the subtype of semi-humid evergreen broad-leaved forest vegetation in Yunnan Province is mainly distributed in the subtropical plateau of central Yunnan and its northern mountains and its distribution elevation is 1500–2900 m, while HEBF is distributed in southern Yunnan and the low mountains in southwestern Yunnan, and its distribution elevation is 900–2000 m, which is similar to the evergreen broad-leaved forests division in Sichuan Province derived in this study. Additionally, this is now consistent with the so-called elevation effect [83], i.e., the vegetation zone will be elevated in large mountains and depressed in small isolated mountains.

The climate variations in the study area, characterized by warm and humid conditions in the eastern HEBF region and distinct wet and dry seasons in the southwest Sichuan SEBF region, significantly influence the distribution of these vegetation types. Elevation and topography further contribute to their spatial patterns. The HEBF thrives in a warm and humid climate with abundant rainfall, while the SEBF adapts to drier conditions during the dry season. Considering the influence of elevation and topography in the classification process can enhance the accuracy of identifying and mapping the HEBF and SEBF. Elevation influences temperature variations, moisture availability, and solar radiation exposure, which directly impact the distribution of vegetation types. Topographic factors, such as slope and aspect, further modify local microclimates, creating ecological niches for specific vegetation communities [71,84,85]. Incorporating elevation and topographic information allows for a better understanding of the spatial patterns and ecological dynamics of HEBF and SEBF, ultimately improving the precision of vegetation classification in the study area.

## 5. Conclusions

Evergreen broad-leaved forests are essential for maintaining ecological balance and providing important ecological services. Thus, accurate mapping and classification of these forests are necessary to understand their spatial distribution, structure, and composition, as well as to assess their ecological functions and services. However, quantitative and accurate vegetation classification maps for the two subtypes of evergreen broad-leaved forest (HEBF and SEBF) with different vegetation productivity and species composition are still lacking. This study successfully achieved accurate extraction and classification of evergreen broad-leaved forests in Sichuan Province by employing a hierarchy-based classifier. The integration of environmental variables and image features enabled effective and quantitative differentiation of HEBF and SEBF, providing a feasible approach for fine-scale classification of evergreen broad-leaved forests. Topographic correction played a crucial role in mountainous vegetation classification, improving classification accuracy and reliability by mitigating the effects of terrain. This study can provide an effective and more detailed approach to the vegetation classification in mountain areas, as well as to the ecological construction of vegetation, the development of agriculture and animal husbandry, and the construction of ecological zones in Sichuan Province.

**Author Contributions:** Conceptualization, S.Z. and P.P.; methodology, S.Z., M.B. and X.D.; software, M.B., X.W. (Xiao Wang) and J.H.; validation, S.Z. and M.B.; formal analysis, M.B., S.Z., X.W. (Xiao Wang) and J.H.; investigation, X.W. (Xueman Wang), J.W. and S.Z.; resources, P.P., J.W., and X.D.; data curation, X.W. (Xueman Wang); writing—original draft preparation, S.Z., M.B., X.W. (Xiao Wang), D.Z. and X.S.; writing—review and editing, X.D., M.W., S.Z., M.B. and D.Z.; visualization, M.B., S.Z. and X.S.; supervision, P.P., X.D., D.Z., X.S. and L.Z.; project administration, P.P., J.W. and L.Z. All authors have read and agreed to the published version of the manuscript.

**Data Availability Statement:** No new data were created or analyzed in this study. Data sharing is not applicable to this article.

**Conflicts of Interest:** The authors declare no conflict of interest.

# Appendix A

**Table A1.** The number of Landsat 8 OLI serial.

| The Number of Landsat 8 OLI Serial | Dry Seasons Images | Wet Seasons Images |
|---|---|---|
| 1 | LC08_127037_20191203 | LC08_127038_20200831 |
| 2 | LC08_127038_20200120 | LC08_127037_20200714 |
| 3 | LC08_127039_20200324 | LC08_127039_20200714 |
| 4 | LC08_127040_20191101 | LC08_127040_20200714 |
| 5 | LC08_127041_20191101 | LC08_127041_20200831 |
| 6 | LC08_128037_20191226 | LC08_128038_20200907 |
| 7 | LC08_128038_20200111 | LC08_128037_20200603 |
| 8 | LC08_128039_20191210 | LC08_128039_20200907 |
| 9 | LC08_128040_20200111 | LC08_128040_20200907 |
| 10 | LC08_128041_20200212 | LC08_128041_20200603 |
| 11 | LC08_129037_20200219 | LC08_129038_20200712 |
| 12 | LC08_129038_20200219 | LC08_129037_20200813 |
| 13 | LC08_129039_20200219 | LC08_129039_20200728 |
| 14 | LC08_129040_20200219 | LC08_129040_20200728 |
| 15 | LC08_129041_20200219 | LC08_129041_20200728 |
| 16 | LC08_129042_20191217 | LC08_129042_20200728 |
| 17 | LC08_130037_20191122 | LC08_130038_20200719 |
| 18 | LC08_130038_20191208 | LC08_130037_20200719 |
| 19 | LC08_130039_20200210 | LC08_130039_20200703 |
| 20 | LC08_130040_20200226 | LC08_130040_20200703 |
| 21 | LC08_130041_20200226 | LC08_130041_20200601 |
| 22 | LC08_130042_20200313 | LC08_130042_20200601 |
| 23 | LC08_130036_20200313 | LC08_130036_20200719 |
| 24 | LC08_131037_20191231 | LC08_131038_20200624 |
| 25 | LC08_131038_20200116 | LC08_131037_20200624 |
| 26 | LC08_131039_20191215 | LC08_131039_20200827 |
| 27 | LC08_131040_20191215 | LC08_131040_20200827 |
| 28 | LC08_131041_20191129 | LC08_131041_20200827 |
| 29 | LC08_131042_20191129 | LC08_131042_20200827 |
| 30 | LC08_131036_20191231 | LC08_131036_20200624 |
| 31 | LC08_132037_20191206 | LC08_132038_20200903 |
| 32 | LC08_132038_20191206 | LC08_132037_20200903 |
| 33 | LC08_132039_20191206 | LC08_132039_20200903 |
| 34 | LC08_132040_20191206 | LC08_132040_20200903 |
| 35 | LC08_132041_20191206 | LC08_132041_20200701 |
| 36 | LC08_132036_20200107 | LC08_132036_20200802 |
| 37 | LC08_133037_20191229 | LC08_133038_20200825 |
| 38 | LC08_133038_20191229 | LC08_133037_20200825 |
| 39 | LC08_133039_20200114 | LC08_133039_20200825 |
| 40 | LC08_133040_20200114 | LC08_133040_20200825 |
| 41 | LC08_134037_20200325 | LC08_134038_20200901 |
| 42 | LC08_134038_20200325 | LC08_134037_20200917 |
| 43 | LC08_134036_20191102 | LC08_134036_20200917 |

**Table A2.** The number of Sentinel-1 serial.

| The Number of Sentinel-1 Serial | Dry Seasons Images | Wet Seasons Images |
| --- | --- | --- |
| 1 | LC08_127037_20191203 | LC08_127038_20200831 |
| 2 | LC08_127038_20200120 | LC08_127037_20200714 |
| 3 | LC08_127039_20200324 | LC08_127039_20200714 |
| 4 | LC08_127040_20191101 | LC08_127040_20200714 |
| 5 | LC08_127041_20191101 | LC08_127041_20200831 |
| 6 | LC08_128037_20191226 | LC08_128038_20200907 |
| 7 | LC08_128038_20200111 | LC08_128037_20200603 |
| 8 | LC08_128039_20191210 | LC08_128039_20200907 |
| 9 | LC08_128040_20200111 | LC08_128040_20200907 |
| 10 | LC08_128041_20200212 | LC08_128041_20200603 |
| 11 | LC08_129037_20200219 | LC08_129038_20200712 |
| 12 | LC08_129038_20200219 | LC08_129037_20200813 |
| 13 | LC08_129039_20200219 | LC08_129039_20200728 |
| 14 | LC08_129040_20200219 | LC08_129040_20200728 |
| 15 | LC08_129041_20200219 | LC08_129041_20200728 |
| 16 | LC08_129042_20191217 | LC08_129042_20200728 |
| 17 | LC08_130037_20191122 | LC08_130038_20200719 |
| 18 | LC08_130038_20191208 | LC08_130037_20200719 |
| 19 | LC08_130039_20200210 | LC08_130039_20200703 |
| 20 | LC08_130040_20200226 | LC08_130040_20200703 |
| 21 | LC08_130041_20200226 | LC08_130041_20200601 |
| 22 | LC08_130042_20200313 | LC08_130042_20200601 |
| 23 | LC08_130036_20200313 | LC08_130036_20200719 |
| 24 | LC08_131037_20191231 | LC08_131038_20200624 |
| 25 | LC08_131038_20200116 | LC08_131037_20200624 |
| 26 | LC08_131039_20191215 | LC08_131039_20200827 |
| 27 | LC08_131040_20191215 | LC08_131040_20200827 |
| 28 | LC08_131041_20191129 | LC08_131041_20200827 |
| 29 | LC08_131042_20191129 | LC08_131042_20200827 |
| 30 | LC08_131036_20191231 | LC08_131036_20200624 |
| 31 | LC08_132037_20191206 | LC08_132038_20200903 |
| 32 | LC08_132038_20191206 | LC08_132037_20200903 |
| 33 | LC08_132039_20191206 | LC08_132039_20200903 |
| 34 | LC08_132040_20191206 | LC08_132040_20200903 |
| 35 | LC08_132041_20191206 | LC08_132041_20200701 |
| 36 | LC08_132036_20200107 | LC08_132036_20200802 |
| 37 | LC08_133037_20191229 | LC08_133038_20200825 |
| 38 | LC08_133038_20191229 | LC08_133037_20200825 |
| 39 | LC08_133039_20200114 | LC08_133039_20200825 |
| 40 | LC08_133040_20200114 | LC08_133040_20200825 |
| 41 | LC08_134037_20200325 | LC08_134038_20200901 |
| 42 | LC08_134038_20200325 | LC08_134037_20200917 |
| 43 | LC08_134036_20191102 | LC08_134036_20200917 |

**Appendix B**
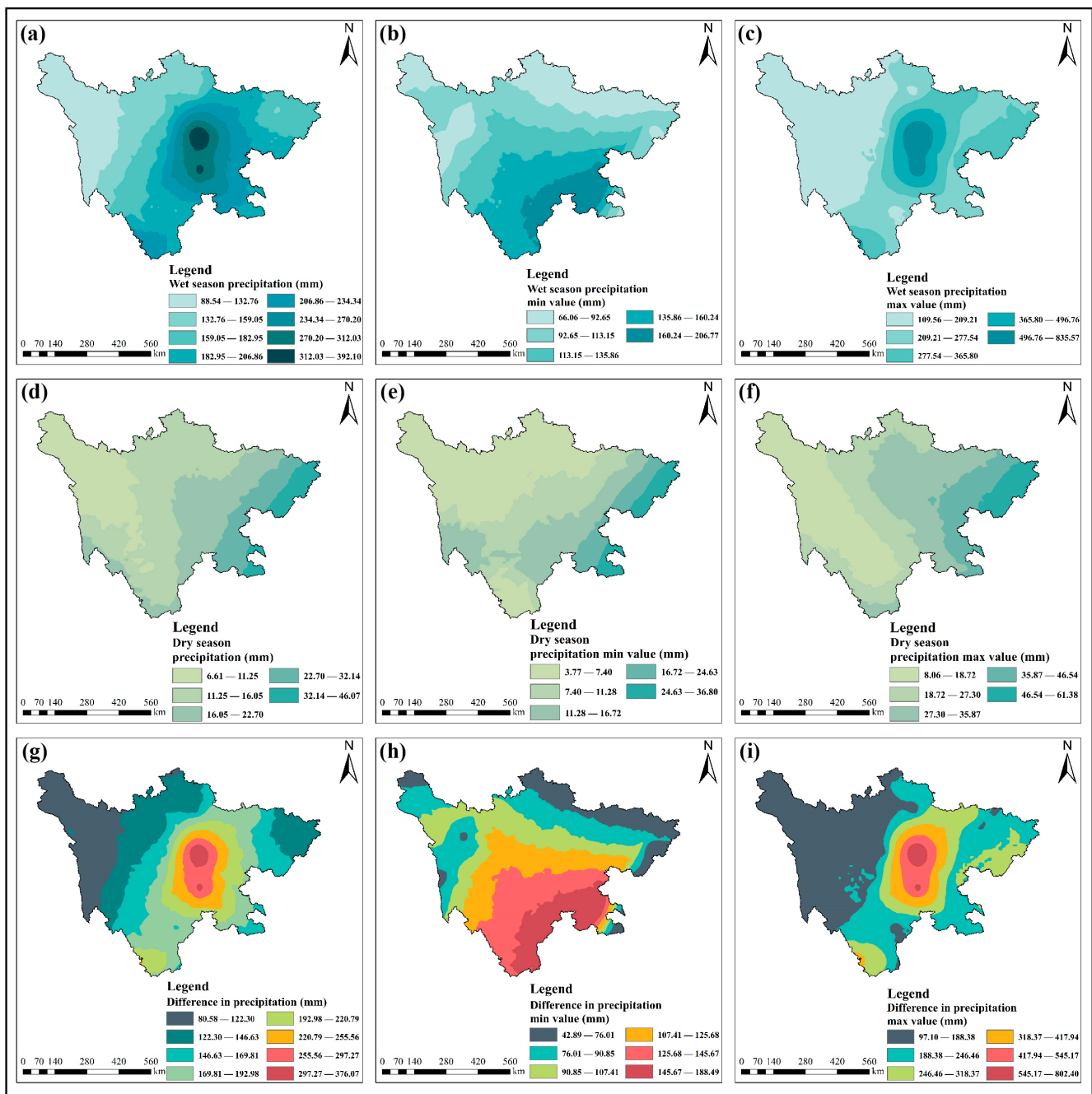


**Figure A1.** Interpolation results of precipitation.(**a**). Mean precipitation during the wet season. (**b**). Minimum precipitation during the wet season. (**c**). Maximum precipitation during the wet season. (**d**). Mean precipitation during the dry season. (**e**). Minimum precipitation during the dry season. (**f**). Maximum precipitation during the dry season. (**g**). Mean difference in precipitation between dry and wet seasons. (**h**). Minimum difference in precipitation between dry and wet seasons. (**i**). Maximum difference in precipitation between dry and wet seasons.
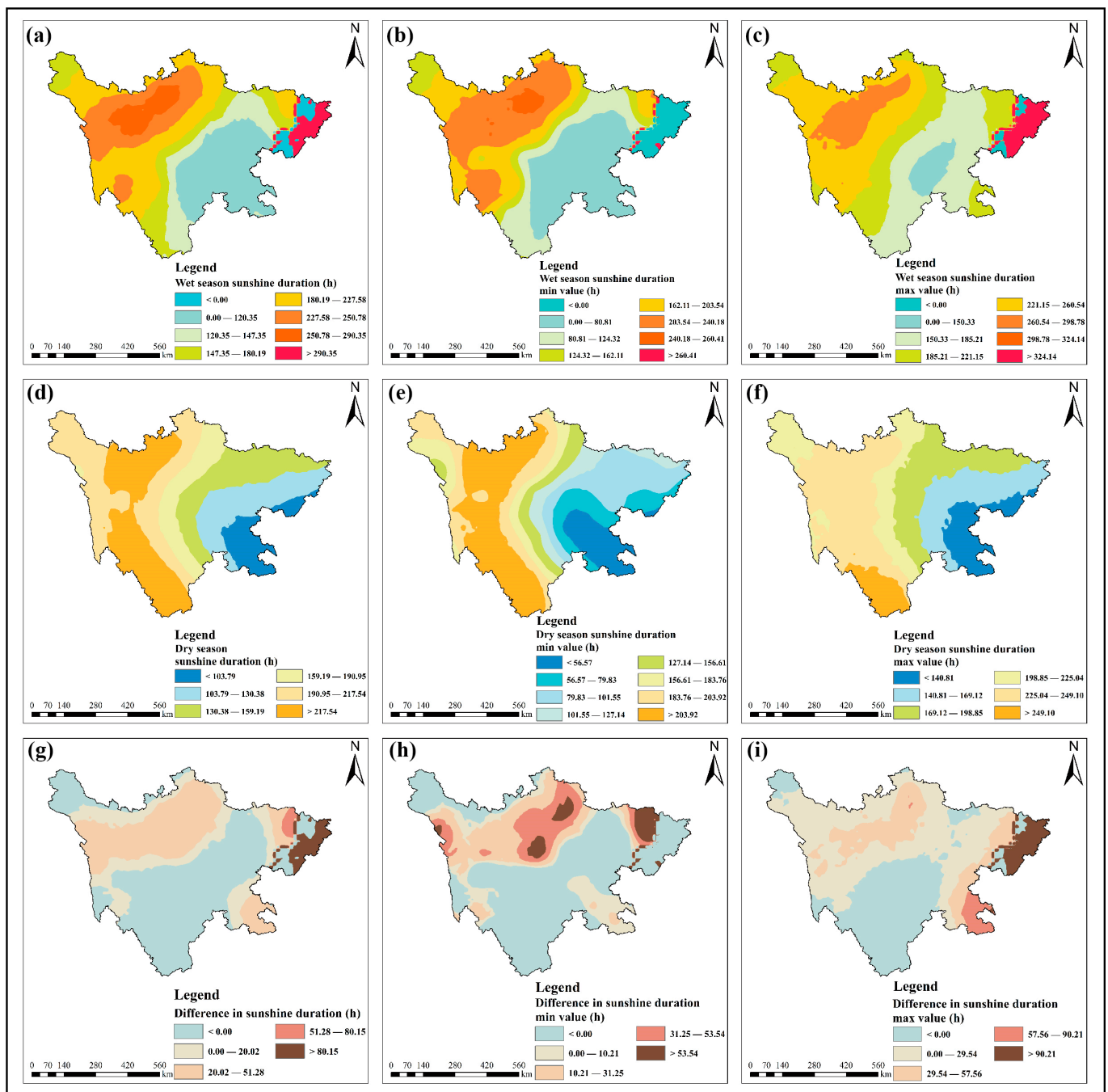
**Figure A2.** Interpolated results of sunshine duration. (**a**). Mean sunshine duration during the wet season. (**b**). Minimum sunshine duration during the wet season. (**c**). Maximum sunshine duration during the wet season. (**d**). Mean sunshine duration during the dry season. (**e**). Minimum sunshine duration during the dry season. (**f**). Maximum sunshine duration during the dry season. (**g**). Mean difference in sunshine duration between dry and wet seasons. (**h**). Minimum difference in sunshine duration between dry and wet seasons. (**i**). Maximum difference in sunshine duration between dry and wet seasons.
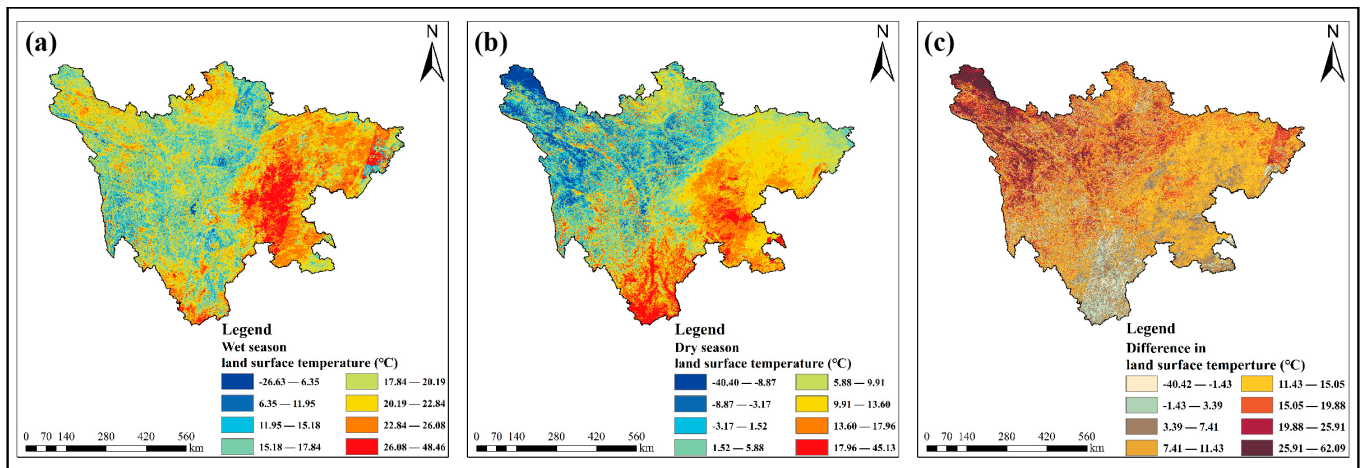
**Figure A3.** Inversion results from land surface temperature. (**a**). Land surface temperature during the wet season. (**b**). Land surface temperature during the wet season. (**c**). Difference in land surface temperature between dry and wet seasons.
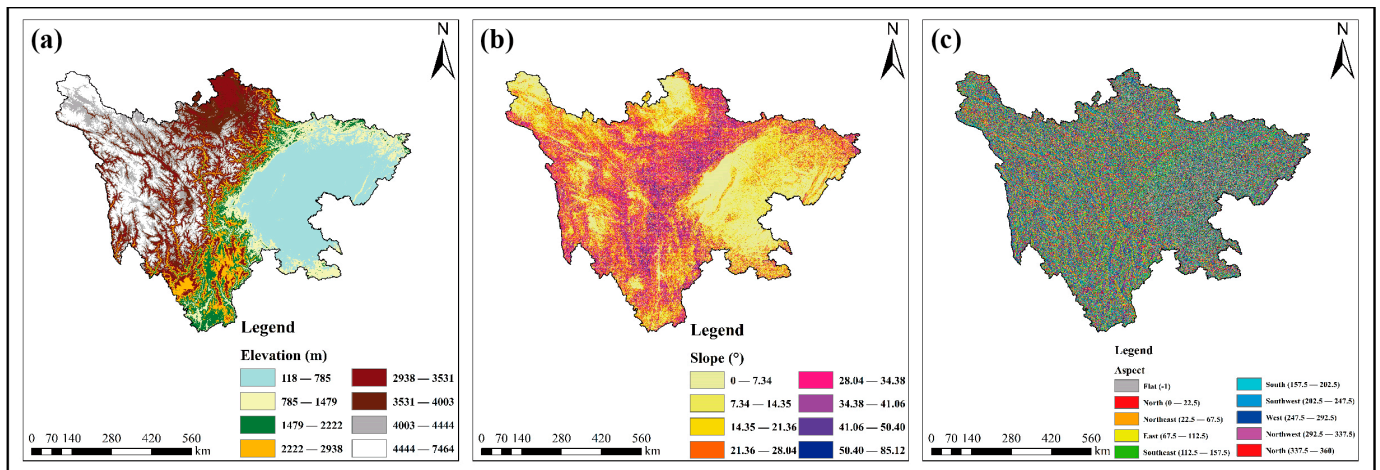


**Figure A4.** Terrain environment variables. (**a**). Elevation in the study area. (**b**). Slope in the study area. (**c**). Aspect in the study area.

**Table A3.** The number of image serial.

| The Number of Landsat 8 OLI Serial | Dry Seasons Images | Wet Seasons Images |
|---|---|---|
| 1 | LC08_127037_20191203 | LC08_127038_20200831 |
| 2 | LC08_127038_20200120 | LC08_127037_20200714 |
| 3 | LC08_127039_20200324 | LC08_127039_20200714 |
| 4 | LC08_127040_20191101 | LC08_127040_20200714 |
| 5 | LC08_127041_20191101 | LC08_127041_20200831 |
| 6 | LC08_128037_20191226 | LC08_128038_20200907 |
| 7 | LC08_128038_20200111 | LC08_128037_20200603 |
| 8 | LC08_128039_20191210 | LC08_128039_20200907 |
| 9 | LC08_128040_20200111 | LC08_128040_20200907 |
| 10 | LC08_128041_20200212 | LC08_128041_20200603 |
| 11 | LC08_129037_20200219 | LC08_129038_20200712 |
| 12 | LC08_129038_20200219 | LC08_129037_20200813 |

**Table A3.** *Cont.*

| The Number of Landsat 8 OLI Serial | Dry Seasons Images | Wet Seasons Images |
|---|---|---|
| 13 | LC08_129039_20200219 | LC08_129039_20200728 |
| 14 | LC08_129040_20200219 | LC08_129040_20200728 |
| 15 | LC08_129041_20200219 | LC08_129041_20200728 |
| 16 | LC08_129042_20191217 | LC08_129042_20200728 |
| 17 | LC08_130037_20191122 | LC08_130038_20200719 |
| 18 | LC08_130038_20191208 | LC08_130037_20200719 |
| 19 | LC08_130039_20200210 | LC08_130039_20200703 |
| 20 | LC08_130040_20200226 | LC08_130040_20200703 |
| 21 | LC08_130041_20200226 | LC08_130041_20200601 |
| 22 | LC08_130042_20200313 | LC08_130042_20200601 |
| 23 | LC08_130036_20200313 | LC08_130036_20200719 |
| 24 | LC08_131037_20191231 | LC08_131038_20200624 |
| 25 | LC08_131038_20200116 | LC08_131037_20200624 |
| 26 | LC08_131039_20191215 | LC08_131039_20200827 |
| 27 | LC08_131040_20191215 | LC08_131040_20200827 |
| 28 | LC08_131041_20191129 | LC08_131041_20200827 |
| 29 | LC08_131042_20191129 | LC08_131042_20200827 |
| 30 | LC08_131036_20191231 | LC08_131036_20200624 |
| 31 | LC08_132037_20191206 | LC08_132038_20200903 |
| 32 | LC08_132038_20191206 | LC08_132037_20200903 |
| 33 | LC08_132039_20191206 | LC08_132039_20200903 |
| 34 | LC08_132040_20191206 | LC08_132040_20200903 |
| 35 | LC08_132041_20191206 | LC08_132041_20200701 |
| 36 | LC08_132036_20200107 | LC08_132036_20200802 |
| 37 | LC08_133037_20191229 | LC08_133038_20200825 |
| 38 | LC08_133038_20191229 | LC08_133037_20200825 |
| 39 | LC08_133039_20200114 | LC08_133039_20200825 |
| 40 | LC08_133040_20200114 | LC08_133040_20200825 |
| 41 | LC08_134037_20200325 | LC08_134038_20200901 |
| 42 | LC08_134038_20200325 | LC08_134037_20200917 |
| 43 | LC08_134036_20191102 | LC08_134036_20200917 |

**Table A4.** Dry and wet seasons images of Sentinel-1 serial number.

| The Number of Sentinel-1 Serial | Dry Seasons Images | Wet Seasons Images |
|---|---|---|
| 1 | LC08_127037_20191203 | LC08_127038_20200831 |
| 2 | LC08_127038_20200120 | LC08_127037_20200714 |
| 3 | LC08_127039_20200324 | LC08_127039_20200714 |
| 4 | LC08_127040_20191101 | LC08_127040_20200714 |
| 5 | LC08_127041_20191101 | LC08_127041_20200831 |
| 6 | LC08_128037_20191226 | LC08_128038_20200907 |
| 7 | LC08_128038_20200111 | LC08_128037_20200603 |
| 8 | LC08_128039_20191210 | LC08_128039_20200907 |
| 9 | LC08_128040_20200111 | LC08_128040_20200907 |
| 10 | LC08_128041_20200212 | LC08_128041_20200603 |
| 11 | LC08_129037_20200219 | LC08_129038_20200712 |
| 12 | LC08_129038_20200219 | LC08_129037_20200813 |
| 13 | LC08_129039_20200219 | LC08_129039_20200728 |
| 14 | LC08_129040_20200219 | LC08_129040_20200728 |
| 15 | LC08_129041_20200219 | LC08_129041_20200728 |
| 16 | LC08_129042_20191217 | LC08_129042_20200728 |

**Table A4.** *Cont.*

| The Number of Sentinel-1 Serial | Dry Seasons Images | Wet Seasons Images |
|---|---|---|
| 17 | LC08_130037_20191122 | LC08_130038_20200719 |
| 18 | LC08_130038_20191208 | LC08_130037_20200719 |
| 19 | LC08_130039_20200210 | LC08_130039_20200703 |
| 20 | LC08_130040_20200226 | LC08_130040_20200703 |
| 21 | LC08_130041_20200226 | LC08_130041_20200601 |
| 22 | LC08_130042_20200313 | LC08_130042_20200601 |
| 23 | LC08_130036_20200313 | LC08_130036_20200719 |
| 24 | LC08_131037_20191231 | LC08_131038_20200624 |
| 25 | LC08_131038_20200116 | LC08_131037_20200624 |
| 26 | LC08_131039_20191215 | LC08_131039_20200827 |
| 27 | LC08_131040_20191215 | LC08_131040_20200827 |
| 28 | LC08_131041_20191129 | LC08_131041_20200827 |
| 29 | LC08_131042_20191129 | LC08_131042_20200827 |
| 30 | LC08_131036_20191231 | LC08_131036_20200624 |
| 31 | LC08_132037_20191206 | LC08_132038_20200903 |
| 32 | LC08_132038_20191206 | LC08_132037_20200903 |
| 33 | LC08_132039_20191206 | LC08_132039_20200903 |
| 34 | LC08_132040_20191206 | LC08_132040_20200903 |
| 35 | LC08_132041_20191206 | LC08_132041_20200701 |
| 36 | LC08_132036_20200107 | LC08_132036_20200802 |
| 37 | LC08_133037_20191229 | LC08_133038_20200825 |
| 38 | LC08_133038_20191229 | LC08_133037_20200825 |
| 39 | LC08_133039_20200114 | LC08_133039_20200825 |
| 40 | LC08_133040_20200114 | LC08_133040_20200825 |
| 41 | LC08_134037_20200325 | LC08_134038_20200901 |
| 42 | LC08_134038_20200325 | LC08_134037_20200917 |
| 43 | LC08_134036_20191102 | LC08_134036_20200917 |

## References

1. Huang, K.; Xia, J. High ecosystem stability of evergreen broadleaf forests under severe droughts. *Glob. Chang. Biol.* **2019**, *25*, 3494–3503. [CrossRef]
2. Chen, X.H.; Xiang, K.L.; Lian, L.; Peng, H.W.; Erst, A.S.; Xiang, X.G.; Chen, Z.D.; Wang, W. Biogeographic diversification of Mahonia (Berberidaceae): Implications for the origin and evolution of East Asian subtropical evergreen broadleaved forests. *Mol. Phylogenetics Evol.* **2020**, *151*, 106910. [CrossRef]
3. Hai, L.; Li, X.Q.; Zhang, J.B.; Xiang, X.G.; Li, R.Q.; Jabbour, F.; Ortiz, R.d.C.; Lu, A.M.; Chen, Z.D.; Wang, W. Assembly dynamics of East Asian subtropical evergreen broadleaved forests: New insights from the dominant Fagaceae trees. *J. Integr. Plant Biol.* **2022**, *64*, 2126–2134. [CrossRef] [PubMed]
4. Zhou, G.; Houlton, B.Z.; Wang, W.; Huang, W.; Xiao, Y.; Zhang, Q.; Liu, S.; Cao, M.; Wang, X.; Wang, S.; et al. Substantial reorganization of China's tropical and subtropical forests: Based on the permanent plots. *Glob. Chang. Biol.* **2014**, *20*, 240–250. [CrossRef] [PubMed]
5. Zhou, G.; Wei, X.; Wu, Y.; Liu, S.; Huang, Y.; Yan, J.; Zhang, D.; Zhang, Q.; Liu, J.; Meng, Z.; et al. Quantifying the hydrological responses to climate change in an intact forested small watershed in Southern China. *Glob. Chang. Biol.* **2011**, *17*, 3736–3746. [CrossRef]
6. Wang, W.; Wang, J.; Liu, X.; Zhou, G.; Yan, J. Decadal drought deaccelerated the increasing trend of annual net primary production in tropical or subtropical forests in southern China. *Sci. Rep.* **2016**, *6*, 28640. [CrossRef] [PubMed]
7. Fang, J.Y.; Song, Y.C.; Liu, H.Y.; Piao, S.L. Vegetation-climate relationship and its application in the division of vegetation zone in China. *Acta Bot. Sin.* **2002**, *44*, 1105–1122.
8. Song, Y. Tentative classification scheme of evergreen broad-leaved forest of China. *Acta Phytoecol. Sin.* **2004**, *28*, 435–448.
9. Sun, S. Concrning the Vegetation Chinese Regionalization Map as a Part of the Natural Geographical Atlas of the Peoples Republic of China. *Chin. J. Plant Ecol.* **1998**, *22*, 523–537.
10. Song, Y.; Yan, E.; Song, K. Synthetic comparison of eight dynamics plots in evergreen broadleaf forests, China. *Biodivers. Sci.* **2015**, *23*, 139–148. [CrossRef]
11. Peng, S.; You, W.; Zheng, Z.; Wang, L. Effects of recent 60 years climate change on net primary productivity of evergreen broadleaved forest in Tiantong region of Zhejiang Province. *Chin. J. Ecol.* **2011**, *30*, 502–507.
12. Xu, F.; Jiao, H.; Ding, X.; Ye, Q.; Chen, F.; Lin, Y. Spatialtemporal Characteristics of NPP in Subtropical Evergreen Broad-leaved Forests. *J. Northwest For. Univ.* **2019**, *34*, 62–68.

13. Qiao, L.; Schaefer, D.A.; Zou, X. Variations in net litter nutrient input associated with tree species influence on soil nutrient contents in a subtropical evergreen broad-leaved forest. *Chin. Sci. Bull.* **2014**, *59*, 46–53. [CrossRef]

14. Zhu, J.; Wu, A.; Zou, S.; Xiong, X.; Liu, S.; Chu, G.; Zhang, Q.; Liu, J.; Tang, X.; Yan, J.; et al. Relationships between tree diversity and biomass/productivity and their influence factors in a lower subtropical evergreen broad-leaved forest. *Biodivers. Sci.* **2021**, *29*, 1435–1446. [CrossRef]

15. Franklin, S. How a national vegetation classification can help ecological research and management. *Front. Ecol. Environ.* **2015**, *13*, 185–186. [CrossRef]

16. Grime, J.P. Vegetation classification by reference to strategies. *Nature* **1974**, *250*, 26–31. [CrossRef]

17. Wan, H.; Tang, Y.; Jing, L.; Li, H.; Qiu, F.; Wu, W. Tree species classification of forest stands using multisource remote sensing data. *Remote Sens.* **2021**, *13*, 144. [CrossRef]

18. Fassnacht, F.E.; Latifi, H.; Stereńczak, K.; Modzelewska, A.; Lefsky, M.; Waser, L.T.; Straub, C.; Ghosh, A. Review of studies on tree species classification from remotely sensed data. *Remote Sens. Environ.* **2016**, *186*, 64–87. [CrossRef]

19. Xu, E.; Cuo, Y.; Chen, E.; Li, Z.; Zhao, L.; Liu, Q. An Estimation Model for Regional Forest Canopy Closure Combined with UAV LiDAR and High Spatial Resolution Satellite Remote Sensing Data. *Geomat. Inf. Sci. Wuhan Univ.* **2022**, *47*, 1298–1308.

20. Zhang, X.; Liu, L.; Chen, X.; Gao, Y.; Xie, S.; Mi, J. GLC_FCS30: Global land-cover product with fine classification system at 30 m using time-series Landsat imagery. *Earth Syst. Sci. Data* **2021**, *13*, 2753–2776. [CrossRef]

21. Friedl, M.A.; Sulla-Menashe, D.; Tan, B.; Schneider, A.; Ramankutty, N.; Sibley, A.; Huang, X. MODIS Collection 5 global land cover: Algorithm refinements and characterization of new datasets. *Remote Sens. Environ.* **2010**, *114*, 168–182. [CrossRef]

22. Chen, J.; Chen, J.; Liao, A.; Cao, X.; Chen, L.; Chen, X.; He, C.; Han, G.; Peng, S.; Lu, M.; et al. Global land cover mapping at 30 m resolution: A POK-based operational approach. *ISPRS J. Photogramm. Remote Sens.* **2015**, *103*, 7–27. [CrossRef]

23. Bhatnagar, S.; Gill, L.; Regan, S.; Naughton, O.; Johnston, P.; Waldren, S.; Ghosh, B. Mapping Vegetation Communities Inside Wetlands Using Sentinel-2 Imagery in Ireland. *Int. J. Appl. Earth Obs. Geoinf.* **2020**, *88*, 102083. [CrossRef]

24. Wakulińska, M.; Marcinkowska-Ochtyra, A. Multi-temporal sentinel-2 data in classification of mountain vegetation. *Remote Sens.* **2020**, *12*, 2696. [CrossRef]

25. Shammi, S.A.; Meng, Q. Use time series NDVI and EVI to develop dynamic crop growth metrics for yield modeling. *Ecol. Indic.* **2021**, *121*, 107124. [CrossRef]

26. Rokni, K.; Musa, T.A. Normalized difference vegetation change index: A technique for detecting vegetation changes using Landsat imagery. *Catena* **2019**, *178*, 59–63. [CrossRef]

27. Zhai, Y.; Roy, D.P.; Martins, V.S.; Zhang, H.K.; Yan, L.; Li, Z. Conterminous United States Landsat-8 top of atmosphere and surface reflectance tasseled cap transformation coefficients. *Remote Sens. Environ.* **2022**, *274*, 112992. [CrossRef]

28. Schmidt, J.; Fassnacht, F.E.; Förster, M.; Schmidtlein, S. Synergetic use of Sentinel-1 and Sentinel-2 for assessments of heathland conservation status. *Remote Sens. Ecol. Conserv.* **2018**, *4*, 225–239. [CrossRef]

29. Mandal, D.; Kumar, V.; Ratha, D.; Dey, S.; Bhattacharya, A.; Lopez-Sanchez, J.M.; McNairn, H.; Rao, Y.S. Dual polarimetric radar vegetation index for crop growth monitoring using sentinel-1 SAR data. *Remote Sens. Environ.* **2020**, *247*, 111954. [CrossRef]

30. Xu, S.; Xu, X.; Blacker, C.; Gaulton, R.; Zhu, Q.; Yang, M.; Yang, G.; Zhang, J.; Yang, Y.; Yang, M.; et al. Estimation of Leaf Nitrogen Content in Rice Using Vegetation Indices and Feature Variable Optimization with Information Fusion of Multiple-Sensor Images from UAV. *Remote Sens.* **2023**, *15*, 854. [CrossRef]

31. Potočnik Buhvald, A.; Račič, M.; Immitzer, M.; Oštir, K.; Veljanovski, T. Grassland Use Intensity Classification Using Intra-Annual Sentinel-1 and -2 Time Series and Environmental Variables. *Remote Sens.* **2022**, *14*, 3387. [CrossRef]

32. Zeferino, L.B.; Souza, L.F.T.d.; Amaral, C.H.d.; Fernandes Filho, E.I.; de Oliveira, T.S. Does environmental data increase the accuracy of land use and land cover classification? *Int. J. Appl. Earth Obs. Geoinf.* **2020**, *91*, 102128. [CrossRef]

33. Liu, K.; Shi, W.; Zhang, H. A fuzzy topology-based maximum likelihood classification. *ISPRS J. Photogramm. Remote Sens.* **2011**, *66*, 103–114. [CrossRef]

34. Li, H.; Wan, J.; Liu, S.; Sheng, H.; Xu, M. Wetland Vegetation Classification through Multi-Dimensional Feature Time Series Remote Sensing Images Using Mahalanobis Distance-Based Dynamic Time Warping. *Remote Sens.* **2022**, *14*, 501. [CrossRef]

35. Kwan, C.; Gribben, D.; Ayhan, B.; Li, J.; Bernabe, S.; Plaza, A. An accurate vegetation and non-vegetation differentiation approach based on land cover classification. *Remote Sens.* **2020**, *12*, 3880. [CrossRef]

36. Niazmardi, S.; Homayouni, S.; Safari, A.; McNairn, H.; Shang, J.; Beckett, K. Histogram-based spatio-temporal feature classification of vegetation indices time-series for crop mapping. *Int. J. Appl. Earth Obs. Geoinf.* **2018**, *72*, 34–41. [CrossRef]

37. Wan, R.; Wang, P.; Wang, X.; Yao, X.; Dai, X. Mapping Aboveground Biomass of Four Typical Vegetation Types in the Poyang Lake Wetlands Based on Random Forest Modelling and Landsat Images. *Front. Plant Sci.* **2019**, *10*, 1281. [CrossRef] [PubMed]

38. Barrett, B.; Raab, C.; Cawkwell, F.; Green, S. Upland vegetation mapping using Random Forests with optical and radar satellite data. *Remote Sens. Ecol. Conserv.* **2016**, *2*, 212–231. [CrossRef] [PubMed]

39. Friedman, J.H. Greedy Function Approximation: A Gradient Boosting Machine. *Ann. Stat.* **2001**, *29*, 1189–1232. [CrossRef]

40. Jeong, M.; Nam, J.; Ko, B.C. Lightweight Multilayer Random Forests for Monitoring Driver Emotional Status. *IEEE Access* **2020**, *8*, 60344–60354. [CrossRef]

41. Zhao, S.; Jiang, X.; Li, G.; Chen, Y.; Lu, D. Integration of ZiYuan-3 multispectral and stereo imagery for mapping urban vegetation using the hierarchy-based classifier. *Int. J. Appl. Earth Obs. Geoinf.* **2021**, *105*, 102594. [CrossRef]

42. Guo, S.; Zhao, H. Hierarchical classification with multi-path selection based on granular computing. *Artif. Intell. Rev.* **2021**, *54*, 2067–2089. [CrossRef]

43. Zhao, S.; Han, Y.; Zou, Q.; Hu, Q. Hierarchical support vector machine based structural classification with fused hierarchies. *Neurocomputing* **2016**, *214*, 86–92. [CrossRef]

44. Chen, Y.; Zhao, S.; Xie, Z.; Lu, D.; Chen, E. Mapping multiple tree species classes using a hierarchical procedure with optimized node variables and thresholds based on high spatial resolution satellite data. *GIScience Remote Sens.* **2020**, *57*, 526–542. [CrossRef]

45. Cerri, R.; Barros, R.C.; De Carvalho, A.C.P.L.F. Hierarchical multi-label classification using local neural networks. *J. Comput. Syst. Sci.* **2014**, *80*, 39–56. [CrossRef]

46. Sola, I.; González-Audícana, M.; Álvarez-Mozos, J. Multi-criteria evaluation of topographic correction methods. *Remote Sens. Environ.* **2016**, *184*, 247–262. [CrossRef]

47. Huang, B.; Zhao, B.; Song, Y. Urban land-use mapping using a deep convolutional neural network with high spatial resolution multispectral remote sensing imagery. *Remote Sens. Environ.* **2018**, *214*, 73–86. [CrossRef]

48. Liu, X.; Jiang, H.; Wang, X. Extraction of mountain vegetation information based on vegetation distinguished and shadow eliminated vegetation index. *Trans. Chin. Soc. Agric. Eng.* **2019**, *35*, 135–144.

49. Markert, K.N.; Markert, A.M.; Mayer, T.; Nauman, C.; Haag, A.; Poortinga, A.; Bhandari, B.; Thwal, N.S.; Kunlamai, T.; Chishtie, F.; et al. Comparing Sentinel-1 surface water mapping algorithms and radiometric terrain correction processing in southeast Asia utilizing Google Earth Engine. *Remote Sens.* **2020**, *12*, 2469. [CrossRef]

50. Young, N.E.; Anderson, R.S.; Chignell, S.M.; Vorster, A.G.; Lawrence, R.; Evangelista, P.H. A survival guide to Landsat preprocessing. *Ecology* **2017**, *98*, 920–932. [CrossRef]

51. Ma, Y.; He, T.; Li, A.; Li, S. Evaluation and intercomparison of topographic correction methods based on landsat images and simulated data. *Remote Sens.* **2021**, *13*, 4120. [CrossRef]

52. Vanonckelen, S.; Lhermitte, S.; Van Rompaey, A. The effect of atmospheric and topographic correction methods on land cover classification accuracy. *Int. J. Appl. Earth Obs. Geoinf.* **2013**, *24*, 9–21. [CrossRef]

53. Yin, H.; Tan, B.; Frantz, D.; Radeloff, V.C. Integrated topographic corrections improve forest mapping using Landsat imagery. *Int. J. Appl. Earth Obs. Geoinf.* **2022**, *108*, 102716. [CrossRef]

54. Yin, G.; Li, A.; Wu, S.; Fan, W.; Zeng, Y.; Yan, K.; Xu, B.; Li, J.; Liu, Q. PLC: A simple and semi-physical topographic correction method for vegetation canopies based on path length correction. *Remote Sens. Environ.* **2018**, *215*, 184–198. [CrossRef]

55. Jiang, H.; Jia, K.; Zhao, X.; Wei, X.; Wang, B.; Yao, Y.; Zhang, X.; Jiang, B. Review on the theory, method, and research progress of leaf area index estimation in mountainous areas. *J. Remote Sens.* **2020**, *24*, 1433–1449.

56. Guo, Y.; Wu, T.; Luo, J.; Shi, H.; Hao, L. Remote Sensing Mapping of Mountain Vegetation Via Uncertainty-based Iterative Optimization. *J. Geo-information Sci.* **2022**, *24*, 1406–1419. [CrossRef]

57. Soenen, S.A.; Peddle, D.R.; Coburn, C.A. SCS+C: A modified sun-canopy-sensor topographic correction in forested terrain. *IEEE Trans. Geosci. Remote Sens.* **2005**, *43*, 2148–2159. [CrossRef]

58. Ermida, S.L.; Soares, P.; Mantas, V.; Göttsche, F.M.; Trigo, I.F. Google earth engine open-source code for land surface temperature estimation from the landsat series. *Remote Sens.* **2020**, *12*, 1471. [CrossRef]

59. Dong, C.; Zhao, G.; Meng, Y.; Li, B.; Peng, B. The Effect of Topographic Correction on Forest Tree Species Classification Accuracy. *Remote Sens.* **2020**, *12*, 787. [CrossRef]

60. Fang, J.Y.; Yoda, K. Climate and vegetation in China V. Effect of climatic factors on the upper limit of distribution of evergreen broadleaf forest. *Ecol. Res.* **1991**, *6*, 113–125. [CrossRef]

61. He, J.; Chen, W.; Li, J. Community diversity of the main types of the evergreen broad-leaved forest in the eastern part of the middle subtropical China. *Acta Phytoecol. Sin.* **1998**, *22*, 303–311.

62. Song, Y.; Chen, X.; Wang, X. Studies on Evergreen Broad-leaved Forests of China: A Retrospect and Prospect. *J. East China Norm. Univ.* **2005**, *1*, 1–9.

63. Collaborative, S.V. *Vegetation in Sichuan*; Sichuan People's Publishing House: Chengu, China, 1980.

64. Miller, D.L.; Alonzo, M.; Meerdink, S.K.; Allen, M.A.; Tague, C.L.; Roberts, D.A.; McFadden, J.P. Seasonal and interannual drought responses of vegetation in a California urbanized area measured using complementary remote sensing indices. *ISPRS J. Photogramm. Remote Sens.* **2022**, *183*, 178–195. [CrossRef]

65. Mullissa, A.; Vollrath, A.; Odongo-Braun, C.; Slagter, B.; Balling, J.; Gou, Y.; Gorelick, N.; Reiche, J. Sentinel-1 sar backscatter analysis ready data preparation in google earth engine. *Remote Sens.* **2021**, *13*, 1954. [CrossRef]

66. Haralick, R.M.; Dinstein, I.; Shanmugam, K. Textural Features for Image Classification. *IEEE Trans. Syst. Man Cybern.* **1973**, *SMC-3*, 610–621. [CrossRef]

67. Garg, M.; Dhiman, G. A novel content-based image retrieval approach for classification using GLCM features and texture fused LBP variants. *Neural Comput. Appl.* **2021**, *33*, 1311–1328. [CrossRef]

68. Johnstone, I.M.; Paul, D. PCA in High Dimensions: An Orientation. *Proc. IEEE* **2018**, *106*, 1277–1292. [CrossRef] [PubMed]

69. Zhou, Z.; Plauborg, F.; Thomsen, A.G.; Andersen, M.N. A RVI/LAI-reference curve to detect N stress and guide N fertigation using combined information from spectral reflectance and leaf area measurements in potato. *Eur. J. Agron.* **2017**, *87*, 1–7. [CrossRef]

70. Fang, M.; Ju, W.; Zhan, W.; Cheng, T.; Qiu, F.; Wang, J. A new spectral similarity water index for the estimation of leaf water content from hyperspectral data of leaves. *Remote Sens. Environ.* **2017**, *196*, 13–27. [CrossRef]

71. Lampela, M.; Jauhiainen, J.; Kämäri, I.; Koskinen, M.; Tanhuanpää, T.; Valkeapää, A.; Vasander, H. Ground surface microtopography and vegetation patterns in a tropical peat swamp forest. *Catena* **2016**, *139*, 127–136. [CrossRef]

72. Zheng, Y.; Yang, Q.; Ren, H.; Wang, D.; Zhao, C.; Zhao, W. Spatial pattern variation of artificial sand-binding vegetation based on UAV imagery and its influencing factors in an oasis–desert transitional zone Ying. *Ecol. Indic. J.* **2022**, *141*, 109068. [CrossRef]

73. Hagedorn, F.; Gavazov, K.; Alexander, J.M. Above- And belowground linkages shape responses of mountain vegetation to climate change. *Science* **2019**, *365*, 1119–1123. [CrossRef] [PubMed]

74. Niu, Y.; Yang, S.; Zhou, J.; Chu, B.; Ma, S.; Zhu, H.; Hua, L. Vegetation distribution along mountain environmental gradient predicts shifts in plant community response to climate change in alpine meadow on the Tibetan Plateau. *Sci. Total Environ.* **2019**, *650*, 505–514. [CrossRef] [PubMed]

75. Fan, M.; Liao, K.; Lu, D.; Li, D. Examining Vegetation Change and Associated Spatial Patterns in Wuyishan National Park at Different Protection Levels. *Remote Sens.* **2022**, *14*, 1712. [CrossRef]

76. Corney, P.M.; Duc, M.G.L.; Smart, S.M.; Kirby, K.J.; Bunce, R.G.H.; Marrs, R.H. Relationships between the species composition of forest field-layer vegetation and environmental drivers, assessed using a national scale survey. *J. Ecol.* **2006**, *94*, 383–401. [CrossRef]

77. Lou, J.; Xu, G.; Wang, Z.; Yang, Z.; Ni, S. Multi-year ndvi values as indicator of the relationship between spatiotemporal vegetation dynamics and environmental factors in the qaidam basin, china. *Remote Sens.* **2021**, *13*, 1240. [CrossRef]

78. Tassi, A.; Gigante, D.; Modica, G.; Di Martino, L.; Vizzari, M. Pixel-vs. Object-based landsat 8 data classification in google earth engine using random forest: The case study of maiella national park. *Remote Sens.* **2021**, *13*, 2299. [CrossRef]

79. De Frenne, P.; Lenoir, J.; Luoto, M.; Scheffers, B.R.; Zellweger, F.; Aalto, J.; Ashcroft, M.B.; Christiansen, D.M.; Decocq, G.; De Pauw, K.; et al. Forest microclimates and climate change: Importance, drivers and future research agenda. *Glob. Chang. Biol.* **2021**, *27*, 2279–2297. [CrossRef]

80. Aalto, J.; Tyystjärvi, V.; Niittynen, P.; Kemppinen, J.; Rissanen, T.; Gregow, H.; Luoto, M. Microclimate temperature variations from boreal forests to the tundra. *Agric. For. Meteorol.* **2022**, *323*, 109037. [CrossRef]

81. Liu, Y.; Tian, B.; Ou, G. Displacement distribution and climax explanation on semi-humid and humid evergreen broadleaved forests using niche analysis of *Cyclobalanopsis glauca* and *C. glaucoides* in China. *Guihaia* **2022**, *42*, 460–469. [CrossRef]

82. Hua, Z.H.U. Vegetation geography of evergreen broad-leaved forests in Yunnan, southwestern China. *Chin. J. Plant Ecol.* **2021**, *45*, 224–241. [CrossRef]

83. Grubb, P.J. Interpretation of the "Massenerhebung" effect on tropical mountains. *Nature* **1971**, *229*, 44–45. [CrossRef] [PubMed]

84. Fan, J.; Xu, Y.; Ge, H.; Yang, W. Vegetation growth variation in relation to topography in Horqin Sandy Land. *Ecol. Indic.* **2020**, *113*, 106215. [CrossRef]

85. Wang, R.; Wang, Y.; Yan, F. Vegetation Growth Status and Topographic Effects in Frozen Soil Regions on the Qinghai–Tibet Plateau. *Remote Sens.* **2022**, *14*, 4830. [CrossRef]